



1 **BAYESIAN PHYSICAL-STATISTICAL RETRIEVAL OF SWE AND SNOW DEPTH FROM X**
2 **AND KU-BAND SAR - DEMONSTRATION USING AIRBORNE SNOWSAR IN SNOWEX'17**

3 Siddharth Singh¹, Michael Durand,² Edward Kim³, Ana P. Barros¹

4
5 ¹Department of Civil and Environmental Engineering, University of Illinois at Urbana-
6 Champaign, Urbana, Illinois, USA

7 ²School of Earth Sciences, Ohio State University, Columbus, Ohio, USA

8 ³NASA Goddard Space Flight Center, Greenbelt, Maryland, USA

9 *Correspondence to:* Ana P. Barros (barros@illinois.edu)

10 **Abstract**

11 A physical-statistical framework to estimate Snow Water Equivalent (SWE) and snow depth from
12 SAR measurements is presented and applied to four SnowSAR flight-line data sets collected
13 during the SnowEx'2017 field campaign in Grand Mesa, Colorado, USA. The physical (radar)
14 model is used to describe the relationship between snowpack conditions and volume backscatter.
15 The statistical model is a Bayesian inference model that seeks to estimate the joint probability
16 distribution of volume backscatter measurements, snow density and snow depth, and physical
17 model parameters. Prior distributions are derived from multilayer snow hydrology predictions
18 driven by downscaled numerical weather prediction (NWP) forecasts. To reduce noise to signal
19 ratio, SnowSAR measurements at 1 m resolution were upsampled by simple averaging to 30 and 90
20 m resolution. To reduce the number of physical parameters, the multilayer snowpack is
21 transformed for Bayesian inference into an equivalent single- or two-layer snowpack with the same
22 snow mass and volume backscatter. Successful retrievals, defined by absolute convergence
23 backscatter errors ≤ 1.2 dB and local SnowSAR incidence angles between 30° and 45° for X- and
24 Ku-band VV-pol backscatter measurements, were achieved for 75% to 87% for all grassland
25 pixels with SWE up to 0.7m and snow depth up to 2 m. SWE retrievals compare well with snow
26 pit observations showing strong skill in deep snow with average absolute SWE residuals of 5-7%
27 (15-18%) for the two-layer (single-layer) retrieval algorithm. Furthermore, the spatial
28 distributions of snow depth retrievals vis-à-vis LIDAR estimates have Bhattacharya Coefficients
29 above 94% (90%) for grassland pixels at 30 m (90 m resolution), and values up to 76% in mixed
30 forest and grassland areas indicating that the retrievals closely capture snowpack spatial variability.
31 Because NWP forecasts are available everywhere, the proposed approach could be applied to SWE
32 and snow depth retrievals from a dedicated global snow mission.
33



34 1. Introduction

35 The seasonal snowpack plays a critical role in climate and weather variability due to its role in the
36 surface energy budget on account of its high albedo, and in the surface water budget providing
37 temporary storage of frozen precipitation in the cold season until it melts in the warm season and
38 becomes available as runoff. The water stored in the snowpack is measured by the Snow Water
39 Equivalent (SWE), the depth of liquid water per unit area that would be released if the snowpack
40 were to melt completely. It is the product of the specific gravity of snow with respect to water
41 ($\rho_{\text{snow}}/\rho_{\text{w}}$) and the depth of the snowpack (SD). To map SWE in the cold season is to map snow
42 water resources. To map onset of melt and snow wetness is to map the timing and geography of
43 snow water resources availability. Climate variability and change with increasing air temperature,
44 shifts in atmospheric moisture convergence patterns, and increases in the frequency of extreme
45 events is already causing significant changes in frequency and patterns and timing of seasonal
46 snow accumulation and melt with severe implications for water and food security in addition to
47 cascading economic and ecosystem impacts (Huang and Swain, 2022; Musselman et al., 2021;
48 Sturm et al., 2010).

49 The need to capture snowpack heterogeneity and dynamics tied to weather, climate, landcover and
50 landform variability remains a chief challenge to developing a snow observing system at the spatial
51 and temporal scales required to answer water cycle science questions and for societal decision-
52 making. The potential for systematic snowpack monitoring in remote regions has long been
53 investigated, including the integration of remote sensing measurements and physical models (e.g.
54 (Martinec et al. 1991; Mote et al. 2003; Bateni et al. 2015; Li et al. 2017; Kim et al. 2019; Cao and
55 Barros, 2023). Assimilation of radiance or backscatter is most powerful with a time series of
56 observations. Time-series observations are available presently from tower measurements, albeit
57 at the point scale of the tower footprint. Airborne observations can be used for mapping but
58 typically occur once or twice during a winter season and over limited areas. A dedicated satellite
59 mission is necessary to acquire time-series of measurements globally.

60 Presently, advances in radar technology and retrieval algorithms (Tsang et al. 2022), and especially
61 the demonstrated capabilities of NewSpace satellite missions (Villano et al. 2020) make high
62 spatial resolution of Synthetic Aperture Radar (SAR; 10's m) Earth observations from space
63 feasible in contrast to the challenges faced in the past (Rott et al. 2012). During the SnowEx'17
64 field campaign (Kim et al. 2017), a comprehensive data set consisting of airborne dual-frequency
65 SAR (X- and Ku-band Synthetic Aperture Radar) backscatter measurements using the SnowSAR
66 instrument (Macedo et al. 2020), the Airborne Snow Observatory (ASO, Painter et al. 2018) and a
67 plethora of high-quality ground-validation measurements of snowpack properties and ancillary
68 data (Table 1) offer an unprecedented opportunity to investigate the full potential of SAR toward
69 developing the next generation of retrieval algorithms.

70 Due to the highly nonlinear snow physics and the time-varying stratigraphy of snowpacks,
71 radiance or backscatter measurements depend on the vertical structure of snowpack physical
72 properties such as snow density, snow temperature, and snow grain size in addition to SWE and
73 snow depth. Thus, SWE and snow depth retrieval is an underdetermined problem. Physical-
74 statistical approaches enable physically-based constraints to relate measurements to geophysical
75 states and parameters and more directly solving Bayes' law (Berliner, 2003; Kuhnert, 2014). In



76 this manuscript, we propose, implement, demonstrate, and evaluate a general physical-statistical
77 framework to retrieve SWE from SnowSAR measurements across a heterogeneous landscape
78 during SnowEx'17.

79

80 **2. Previous Work**

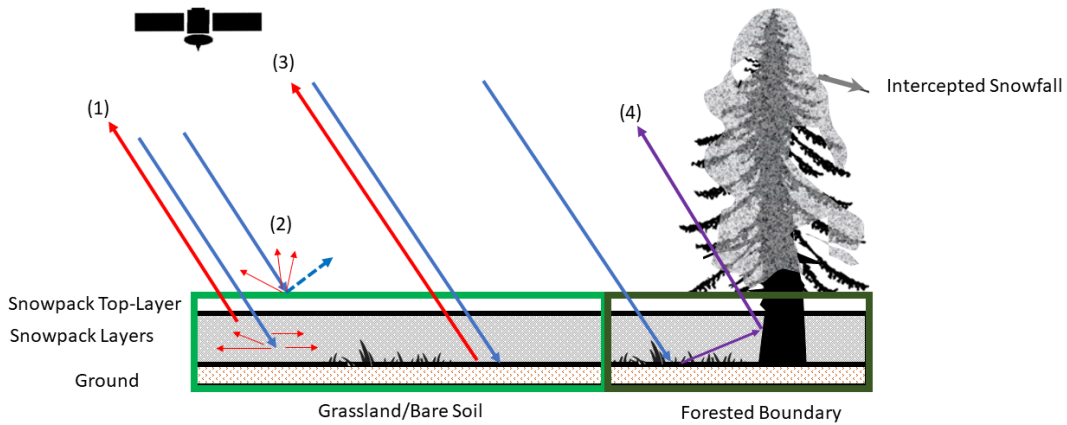
81 **2.1 Forward Simulation - From SWE to Backscatter**

82 The advantage of SAR technology is the high-spatial resolution of its measurements, which is
83 necessary to capture the spatial heterogeneity and temporal variability of snowpack physical
84 processes (e.g. Deems et al. 2016; Mendoza et al., 2020; Manickam and Barros, 2020) as
85 demonstrated in forward simulations. Cao and Barros (2020, 2022; hereafter CB20 and CB22)
86 demonstrated the utility of a coupled multi-layer snow hydrology (MSHM) coupled with a
87 radiative transfer model (RTM) forced by high-resolution operational numerical weather
88 prediction (NWP) model forecasts to capture the seasonal hysteresis behavior of the seasonal
89 snowpack at Grand Mesa and Senator Beck in Colorado against Sentinel-1 C-band measurements.

90 The MSHM is a physically driven snow hydrology model that simulates the evolution of snowpack
91 physical properties including detailed stratigraphy (Kang and Barros, 2012a-b). During snowfall
92 events, fresh snow is added to the top layer of the snowpack until a threshold accumulation is met,
93 and a new layer forms. The RTM used here is MEMLS3a (Microwave Emission Model of Layered
94 Snowpacks adapted to include backscattering by Proksch et al., 2015). MEMLS is a physically
95 driven radiative transfer model which takes snowpack characteristics as inputs and simulates its
96 microwave emission for a frequency band with four polarizations – HH, VV, HV and VH
97 (originally proposed by Wiesmann and Mätzler, 1999). To estimate total scattering, ground
98 backscatter σ_{bkg} must be modeled as well, as described below. .

99 Figure 1 illustrates the various backscatter mechanisms contributing to total backscatter (σ_{total}) in
100 active microwave measurements represented in MEMLS3&a, the RTM: volume backscatter (σ_{vol})
101 from the multiple interactions of the incoming radar signal within the snowpack, the backscatter
102 at the snowpack-air interface (σ_{surf}) and at the snowpack-ground interface including interactions
103 with submerged vegetation and litter (σ_{bkg}). In forested areas, additional backscatter mechanisms
104 are associated with the multiple bounce pathways among tree canopy, intercepted snow, tree
105 trunks, and snowpack. Depending on viewing geometry (flight path and incidence angle), σ_{total}
106 measurements from areas without trees in regions of mixed landcover can include significant
107 contribution from trees along the grassland-forest transitions.

108



109

110 **Figure 1:** Scattering mechanisms for grassland submerged by snow and snowpack over bare soil or rock: (1) Volume Backscatter
 111 σ_{vol} ; (2) surface backscatter σ_{surf} ; (3) background backscatter at the snow-ground interface σ_{bkg} ; (4) snowpack-ground-canopy-tree
 112 trunk interactions at forested boundaries. Red arrows (1), (2) and (3) are resolved in the retrieval applications demonstrated here.

113

114 CB22 used the coupled MSHM-MEMLS in forward mode to predict Sentinel-1 C-band volume
 115 backscatter σ_{vol} without calibration or nudging of ground observations without bias and within \pm
 116 2.5 dB at 90 m resolution across terrain slopes in the $[10^\circ-52^\circ]$ range for barren land and alpine
 117 grass and shrubs and in forested areas with snow-free canopy at the beginning of spring in the
 118 Senator Beck Basin in Colorado. They estimated σ_{bkg} as the average of Sentinel-1 measurements
 119 for snow-free conditions. Cao and Barros (2023) modified MEMLS3&a to include double-bounce
 120 effects among snowpack and vegetation (MEMLS-V) and retrieved σ_{bkg} from total backscatter
 121 σ_{total} measurements in mixed landcover using simulated annealing. Their estimates are consistent
 122 with CB22, suggesting potential to simplify the inverse-problem of estimating snowpack physical
 123 properties from total backscatter measurements in mixed landcover and further simplify the
 124 physical-statistical retrieval framework proposed here, although further evaluation is necessary.

125

126 2.2 Physical-Statistical Retrieval

127 For retrieval in a Bayesian framework, the probability of the retrieved geophysical variable x (the
 128 inferred posterior distribution) is conditional on the *a priori* knowledge of x (the prior distribution),
 129 indirect measurements D , and a physical model $M(\eta)$ (e.g., the snow radiative transfer algorithm
 130 in this case) with physical parameters η (including x) and statistical error parameters ζ . The joint
 131 probability distribution of M , y , η , and ζ can be written as:

$$132 \quad P(M, D, \eta, \zeta) = P(D|M, \eta, \zeta) \times P(M|\eta, \zeta) \times P(\eta, \zeta) \quad (1)$$

133 The first term to the right-hand side of Eq. (1) is the backscatter data model, the second term is the
 134 prior of the backscatter, and the third term is the prior of the snowpack physical parameters
 135 (including snow depth and snow density, etc) with statistical error parameters. Assuming the



136 measurements do not depend on the physical parameters, the model does not depend on the
137 statistical error parameters, and that the physical parameters and the statistical parameters are
138 independent, Eq. (1) can be revised to read

$$139 \quad P(M, D, \eta, \zeta) = P(D|M, \eta) \times P(M|\eta) \times P(\eta) \times P(\zeta) \quad (2)$$

140 And finally in the context of specific measurements y

141

142

$$143 \quad P(M, \eta, \zeta | y) = P(y|M, \eta) \times P(M|\eta) \times \frac{P(\eta) \times P(\zeta)}{P(y)} \quad (3)$$

144 The physical model M and $P(y)$ are invariant and assuming that we have good understanding of
145 the statistical errors, then Eq. (3) can be further simplified as follows

$$146 \quad P(\eta|y) \propto P(y|\eta) \times P(\eta) \quad (4)$$

147

148 In the context of Bayesian inference the goal is to maximize $P(\eta|y)$, the posterior probability of
149 physical parameters conditional on measurements informed by the a priori parameter probabilities
150 $P(\eta)$. To maximize $P(y|\eta)$, the posterior of the backscatter conditional on physical parameters η ,
151 implies minimizing the difference between measurements y with known error covariance matrix
152 Σ_y and model predictions $M(\eta)$. For a multivariate normal distribution, Durand and Liu (2012)
153 proposed

$$154 \quad P(y|\eta) = (2\pi)^{\left(-\frac{N}{2}\right)} |\Sigma_y|^{-\frac{1}{2}} \exp \left[-\frac{1}{2} (y - M(\eta))^T \Sigma_y^{-1} (y - M(\eta)) \right] \quad (5)$$

155 where N is the number of measurements at a given location and time (e.g. backscatter at different
156 frequencies

157 Pan et al. (2023, hereafter P23) adapted a Bayesian retrieval algorithm previously developed to
158 estimate SWE from passive microwave measurements (Pan et al. 2017, hereafter P17) to active
159 microwave, hereafter referred to as Base-AM. The snow radiative transfer algorithm in Base-AM
160 is MEMLS, and the semi-empirical Dobson model is used to estimate the soil dielectric constant
161 as a function of soil moisture and soil texture (Dobson et al. 1985; Hallikainen et al. 1985). A
162 Monte Carlo Markov Chain iterative algorithm (Metropolis et al. 1953) is used to sample from
163 $P(\eta|y)$ starting from initial values. Here, the realistic snowpack predictions from MSHM-MEMLS
164 are used to define the prior distributions of parameters and constrain the Bayesian retrievals.

165

166 **3. Study Area and Data**

167 **3.1 Study Area and Ancillary Data**

168 The study region is Grand Mesa, Colorado, a plateau that is 2,000 m above adjacent low-lying
169 areas and is surrounded by ridges up to 500m in elevation (as depicted in Fig. 2). Grand Mesa



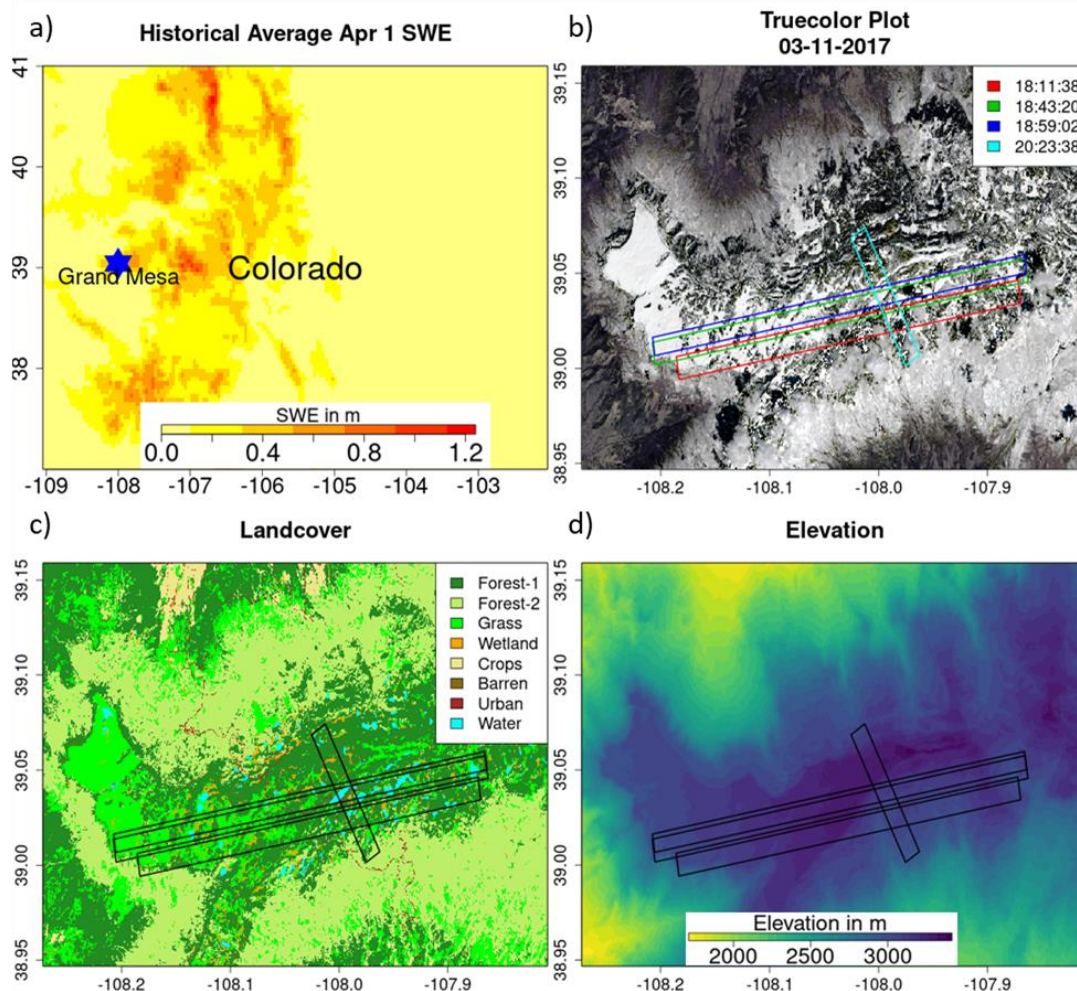
170 has an alpine climate, experiencing snowfall throughout the year except during the months of July
 171 and August. Landcover is heterogeneous with grasslands in the west and a mix of evergreen and
 172 deciduous forest to the east. Numerous wetlands are widespread across the Mesa, especially in the
 173 transition from grassland to forest. The land cover data were obtained from the National Land Data
 174 Assimilation System (NLDAS) and the National American Land Change Monitoring System
 175 (NALCMS), both at 30 m resolution. The datasets were upscaled to 90m using nearest neighbor
 176 interpolation. NLDAS is used to determine landcover type in the snow hydrology model.
 177 NALCMS is used to upscale the evaluation data. Hourly albedo is derived from NLDAS at 12.5
 178 km resolution. A summary of all the datasets used in this study is available in Table 1.

179

180 **Table 1:** Summary list of datasets used in the study.

Data	Source	Spatial Resolution		Temporal Resolution		Date Range	Relevant Link
		Initial	Final	Initial	Final		
Rainfall Temperature Air Pressure Incoming SW radiation Incoming Longwave radiation Wind speed Humidity	HRRR	3 km	30 m, 90 m	1 hr	30 min	9/1/2016 - 2/25/2017	https://rapidrefresh.noaa.gov/hrrr/
Albedo	NLDAS	12.5 km	30 m	1 hr	30 min	9/1/2016-2/25/2017	https://ldas.gsfc.nasa.gov/
Backscatter	SnowSAR – SnowEx’17	1 m	30 m, 90 m	-	-	2/21/2017	https://nsidc.org/data/snex17_snowsar/versions/1
Landcover	NLCD, NALCMS	30 m	30 m, 90 m	-	-	-	https://www.usgs.gov/centers/eros/science/national-land-cover-database http://www.cec.org/north-american-land-change-monitoring-system/
Snow Depth	LIDAR – SnowEx’17	3 m	30 m, 90 m	-	-	2/25/2017	https://nsidc.org/data/snex17_snowpits/versions/1
SWE	Snowpit – SnowEx’17	-	-	-	-	2/20/2017-2/24/2017	https://nsidc.org/data/aso_3m_sd/versions/1

181



182

183 **Figure 2:** Study area in Grand Mesa, Colorado. a) Location of Grand Mesa in Colorado, with historical Apr 1 SWE average as
184 base map. b) Paths of 4 SnowSAR SnowEx'17 flights on 21 Feb 2017, with true color image obtained from Landsat on 03/11/2017
185 as the base map. c) Land cover of the study region. Forest-1 are needle leaf forests; Forest-2 are broadleaf forests. d) Digital
186 elevation map of the study region.

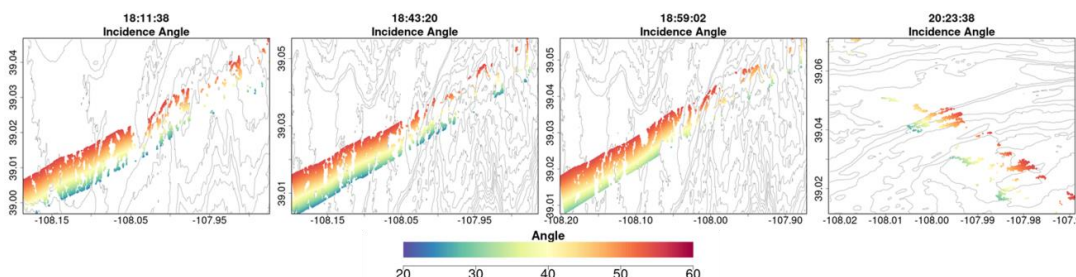
187

188 3.2 Atmospheric Forcing

189 Numerical Weather Prediction (NWP) outputs are used as the atmospheric forcing for the snow
190 hydrology model and to set up boundary conditions. Previously, CB20 and CB22 relied on HRRR
191 (High-Resolution Rapid Refresh) hourly forecasts at 3 km and downscaled it to 90 m in Grand
192 Mesa. Here, the same data set was independently downscaled to 30 m as well. The HRRR dataset
193 is produced by National Ocean and Atmospheric Agency (NOAA) by hourly assimilation of
194 observations at 13 km resolution (Benjamin et al., 2016; Table 1). Hourly atmospheric forcing
195 was linearly interpolated to 30 min temporal resolution used in the snow hydrology model.



196



197

198 **Figure 3:** Maps of incidence angles along SnowSAR flight paths on February 21, 2017 during SnowEx'17.

199

200 **3.4 SnowSAR Backscatter**

201 During SnowEx'17, airborne microwave backscatter measurements were made in Grand Mesa on
202 21 Feb 2017 at 1 m resolution (Table 1). The SnowSAR instrument is a dual frequency (X and Ku
203 Band) radar. A total of six flightlines were completed, two short ones on sloped densely forested
204 terrain and four long lines on the plateau. Here, only the four flightlines on the plateau are used for
205 analysis (Fig. 2 and Fig. 3). The flights are between 18:00 and 21:00 GMT (noon – 3PM MST).
206 SnowSAR data quality control measures included filtering based on aircraft attitude (there were
207 line segments with turbulence), beam incidence angle/antenna pattern, and signal-to-noise-ratio of
208 the backscatter coefficients. Processing of the original airborne SAR measurements and quality
209 control indicate that only the co-pol X-band HH- and VV-pol as well as Ku-band VV-pol
210 measurements are adequate for retrieval. Geolocation was verified against corner reflector targets
211 and geographic features and found to be very robust. The SnowSAR data were upscaled to 30 m
212 and 90 m resolution by simple averaging of all SnowSAR measurements within each pixel.

213

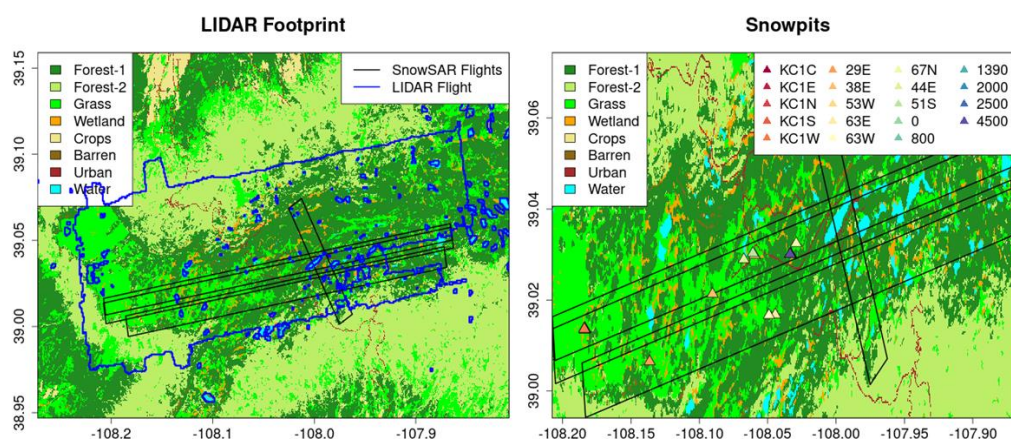
214 **3.5 Validation Data**

215 *LIDAR Snow Depth* – The ASO LIDAR measurements of snow depth at 3m resolution across
216 Grand Mesa are available for SnowEx'17 on February 25, thus 4 days after the SnowSAR flights
217 (Painter et al., 2018; Table 1). There were no significant snow storms or strong winds in that
218 period, except for about 3mm of rainfall for less than 1 hour on February 24 th. These data are
219 used to examine the distribution of retrieved snow depths, that is indicative of the spatial
220 heterogeneity of the snowpack, and the relative absolute differences between LIDAR
221 measurements and retrieval of snow depth, that are indicative of local retrieval errors. The LIDAR
222 data were upscaled to 30 m and 90 m using simple averaging (e.g., Fig.4a). There can be large
223 snow depth underestimation errors associated with upscaled LIDAR retrievals along the edges of
224 forests where the snow depth is underestimated consistent with previous work (e.g. Deems et al.
225 2013; Jacobs et al. 202). Given the expect measurement uncertainty on the order of 10-20 cm in
226 Grand Mesa, which is amplified by microtopography, LIDAR pixels with snow depth shallower
227 than 20 cm are not considered for evaluation.



228 *Snowpit SWE* - Multiple snowpits were excavated during the SnowEx'17 field campaign across
229 Grand Mesa (Table 1). Due to the small number of snow pit measurements along the SnowSAR
230 flightlines on 21 February, snowpit measurements on 20-24 of February were considered for
231 evaluation assuming that in the absence of snowstorms or other weather events the snow pack
232 does not change significantly during the 4-day period. Differences are expected at local places but
233 the overall spatial trends should be maintained such as the west-east gradient in snow depth. The
234 values of snowpit SWE are estimated using an average of the snow density measurements at
235 different depths applied to the entire snow depth. Only pits in non-forested areas were selected
236 for evaluation (Fig. 4b).

237



238

239 **Figure 4:** a) Flight footprint of the LIDAR instrument used to measure the snow depth during SnowEx'17. b) Location of snow
240 pits used to measure SWE 20-24 Feb 2017. The legend identifies SnowEx'17 Pit IDs.

241

242 4. Methods

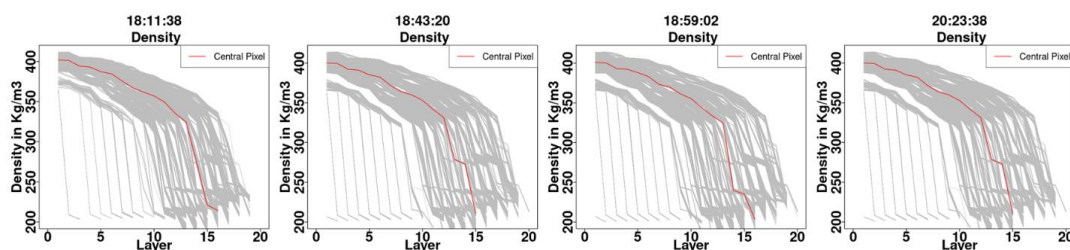
243 4.1 Retrieval Algorithm

244 The retrieval methodology builds on existing and well evaluated snow hydrology, radiative
245 transfer, and physical-statistical models (CB20,CB22, P17, P23) previously reviewed in Section
246 2. Figure 5 illustrates the retrieval workflow consisting of four main steps: **(1a)** Snow hydrology
247 simulation using MSHM to produce a layered snowpack; **(1b)** Volume backscatter σ_{vol} simulation
248 using MEMLS and estimation of background backscatter σ_{bkg} by subtraction from SnowSAR
249 σ_{total} measurements; **(2)** Determination of snowpack parameter prior distributions for retrieval:
250 averaged snowpack physical property distributions for a 1 or 2 layer equivalent snowpack (1|2)
251 with the same mass and total backscatter σ_{total} ; **(3)** Determination of ground priors for retrieval:
252 Bayesian estimation of ground parameters that govern the σ_{bkg} using MEMLS for a very thin (1
253 mm SD) film of snow on the ground; and **(4)** Retrieval: Bayesian optimization of simulated σ_{total}



254 to derive posterior distributions of SD and ρ_{snow} for the 1/2 equivalent snowpack, and subsequent
255 calculation of SWE.

256



257

258 **Figure 5** - Density profiles obtained from MSHM for the 4 SnowSAR flight paths. The density profile of the central pixel for each
259 of the flights is marked in red. Note the significant difference between the top 2-3 layers and the deeper snowpack supporting the
260 two-layer snowpack concept.

261

262 **4.1.1 Layered Snowpack Simulations and Prior Distributions (1a,2)**

263 MSHM was run for a full-year starting from snow free conditions on September 1st 2016 using
264 downscaled HRRR data as atmospheric forcing (Section 1.2) and a timestep of 30 mins. On the
265 day of the SnowSAR flights, the snowpack physical properties predicted at times corresponding
266 to each of the four flights are used to derive the 1/2 Layer equivalent snowpack properties used in
267 the retrieval. Volume backscatter was estimated using the cross polarization fraction $Q=0.2$. The
268 prior distributions for Base-AM are shown in Table 3.

269 In realistic layered snowpacks, stratigraphy (i.e., vertical heterogeneity) is a dominant feature of
270 the density, temperature, microstructure, and dielectric properties (e.g., emissivity and
271 reflectivity). The vertical structure of snow microphysics in MSHM is described using a
272 parameterization of snow correlation length consistent with MEMLS formulation. Depending on
273 the number of layers, this poses an overdetermined problem as the number of measurements is
274 equal to the number of frequencies and the number of polarizations available (typically two or
275 three). For example, there are only four observations for a dual-frequency measurement with dual
276 polarization. In contrast, the set of independent parameters per layer includes snow density, layer
277 thickness, liquid water content, snow grain size or correlation length, temperature, reflectivity, and
278 transmissivity. To reduce the number of independent parameters that need to be estimated, the
279 multilayer snowpack is transformed into an equivalent single- or two-layered snowpack with the
280 same SWE, snow depth (SD) and total backscatter σ_{total} .

281

282

283

284

285

286



287 **Table 2:** Input and output parameters from the three models in the SWE physical-statistical retrieval framework.

Model	Input	Output	Reference
MSHM	Rainfall Temperature Air Pressure Incoming shortwave radiation Incoming longwave radiation Wind speed Humidity Albedo	Snow Temperature Profile Soil Temperature Profile Snow Density Profile Snow Depth Layering Profile Liquid Water Content Profile Snow Correlation Length Profile	Cao and Barros (2020)
MEMLS	Snow Temperature Profile Soil Temperature Profile Snow Density Profile Snow Depth Layering Profile Snow Correlation Length Profile Cross polarization fraction Ground rms height	Diffused Reflectivity Profile Specular Reflectivity Profile Total Backscatter Coefficient	Proksch et al. (2015)
Base AM	Equivalent Snow Temperature Prior Equivalent Soil Temperature Prior Equivalent Snow Density Prior Equivalent Snow Depth Prior Correlation Length Cross polarization fraction Ground rms height Total Backscatter Coefficient Prior	Optimized – Snow Layer Depth Snow Density	Pan et al., 2023

288

289

290

291

292

293

Table 3: Base-AM model input standard deviation and range for the lognormal parameters prepared using MSHM multilayer snowpack parameters. Alphanumerical subscript in 2-layer snowpack retrievals denotes layer number: 1- bottom layer; 2- top layer; avg- the average of all MSHM multilayer parameter values in the corresponding single or 2-layer snowpack. DZ is the MSHM snow depth.

Snow Parameters	1 Layer Snowpack			2 Layer Snowpack			
	Standard Deviation, σ	Range		Standard Deviation, σ		Range for each layer	
		Min	Max	Bottom	Top	Min	Max
Snow Temp., T_s [$^{\circ}\text{C}$]	$0.3 \times T_{s\text{avg}}$	$1.3 \times T_{s\text{min}}$	$0.7 \times T_{s\text{max}}$	$0.3 \times T_{s_{1,\text{avg}}}$	$0.3 \times T_{s_{2,\text{avg}}}$	$1.3 \times T_{s\text{min}}$	$0.7 \times T_{s\text{max}}$
Snow Density, ρ [Kg/m^3]	$0.3 \times \rho_{\text{avg}}$	$0.8 \times \rho_{\text{min}}$	$1.2 \times \rho_{\text{max}}$	$0.3 \times \rho_{1,\text{avg}}$	$0.3 \times \rho_{2,\text{avg}}$	$0.8 \times \rho_{\text{min}}$	$1.2 \times \rho_{\text{max}}$
Snow Depth, DZ [m]	$0.3 \times \text{DZ}$	$0.5 \times \text{DZ}$	$1.5 \times \text{DZ}$	$0.1 \times \text{DZ}_1$	$0.2 \times \text{DZ}_2$	$0.2 \times \text{DZ}$	$0.9 \times \text{DZ}$
Correlation Length, D	$0.3 \times D_{\text{avg}}$	D_{min}	D_{max}	$0.2 \times D_{1,\text{avg}}$	$0.2 \times D_{2,\text{avg}}$	D_{min}	D_{max}
Soil Temp., T_{soil} [$^{\circ}\text{C}$]	0.3	1.3		0.3		1.3	

294

295

296

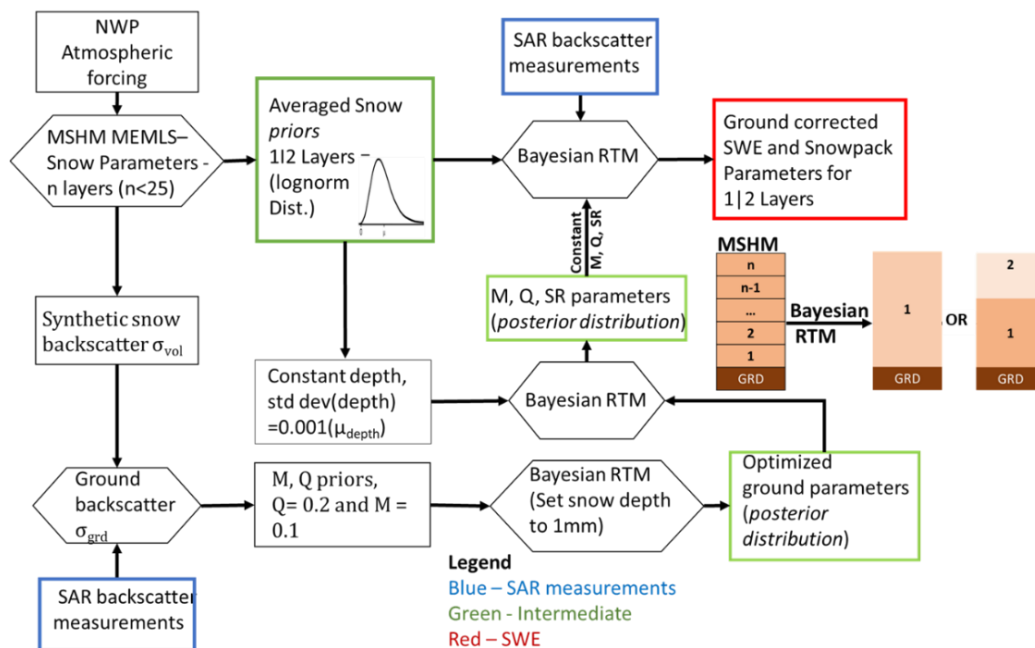
297

Single-layer Snowpack - The total snow depth and the averages of multilayered snowpack parameters are specified as the mean of the prior distribution for retrieval. Table 3 shows the range and standard deviation of the parameters.



298 *Two-layer Snowpack* – The average values of the snowpack physical properties for each of two
 299 layers are derived from the multilayer snowpack simulated by MSHM as for the single-layer case.
 300 The key requirement is to determine the depth of each one of the layers that best captures the
 301 snowpack vertical structure. Figure 5 shows examples of MSHM snow density profiles for each
 302 of the four SnowSAR flights. Note the large changes with depth of the snow density profiles. The
 303 shape of the profiles reflects the interplay between thermodynamic processes that change snow
 304 microstructure and dominate in the upper snowpack and mechanical consolidation processes that
 305 are dominant in the mid and lower layers. The snow depth point corresponding to the maximum
 306 change in snow density between adjacent layers in the multilayer snowpack is used here to divide
 307 the snowpack in two layers. Subsequently, the average density, snow temperature, and correlation
 308 length of the MSHM multilayer snowpack is calculated for the corresponding depths of the two-
 309 layer equivalent snowpack (Table 3).

310



311

312 **Figure 6:** Workflow of the SWE Physical-Statistical retrieval. NWP atmospheric forcings are used to set up MSHM to determine
 313 priors for the Bayesian radiative transfer model (Base-AM) and synthetic backscatter for ground parameters. SnowSAR backscatter
 314 measurements are assimilated to determine the posterior distribution of the snowpack parameters.

315

316 4.1.2 Determination of Ground and Snowpack Microstructure Parameters (1b, 3)

317 A first estimate of the σ_{bkg} is obtained by subtracting σ_{vol} from SnowSAR X-band HH- pol σ_{total}
 318 measurements. In Base-AM, σ_{bkg} depends on the effective effective soil moisture and soil surface
 319 roughness. To optimize these parameters, σ_{bkg} is used as an “observed” value. To simulate snow-



320 free conditions the snow depth is constrained to a maximum value of 1 mm. The cross polarization
321 fraction Q initially specified as $Q=0.2$ is optimized first and separately from other ground
322 parameters in the third step of the retrieval algorithm (Fig. 6). Finally, the posterior distributions
323 of the ground parameters are used along with the 1/2 layer prior distributions and the SnowSAR
324 measurements to estimate the posterior distributions of snow depth and snow density using the
325 Base-AM framework (Fig. 6) and both X- and Ku-band VVpol. SWE is subsequently derived from
326 snow depth and snow density.

327

328 4.2 Retrieval Evaluation

329 The local mean of the posterior distribution for each parameter is hereafter referred to as the
330 retrieval result for each pixel. The retrievals are evaluated against LIDAR snow depth including
331 spatial patterns and gradients, and overall statistical structure using histograms. SWE retrievals
332 derived from the posterior distributions of snow density and snow depth are evaluated against SWE
333 measurements at snowpits (Section 3). Original LIDAR measurements were reprojected and
334 coregistered with the SnowSAR retrievals. A comparative analysis retrievals was conducted to
335 examine the dependence of retrievals on incidence angle for different levels and the subgrid scale
336 variability quantified as the standard deviation of original LIDAR measurements within the
337 upscaled pixel. The amplitude error metrics are the mean, standard deviation, and mean absolute
338 relative error (MARE):

$$339 \quad MARE = \frac{\sum_{i=1}^n |1 - R_i/O_i|}{N} \quad (6)$$

340 where O are observations and R are retrievals. The Bhattacharya coefficient (BC) is used to
341 compare the spatial distributions of snow depth and backscatter. BC measures the similarity
342 between two probability distributions p_1 and p_2 as follows (Bhattacharya, 1943)

343

$$344 \quad BC = \sum_{i=1}^N \sqrt{p_1(i)p_2(i)} \quad (7)$$

345 Finally, among the 39 snowpits available for evaluation on February 21, only 15 pits in open areas
346 (i.e. grasslands) were retained for evaluation and snow pits without SnowSAR measurements
347 within a radius of 100 m were discarded.

348

349 5. Results and Discussion

350 5.1. Successful Retrievals

351 SnowSAR measurements are strongly affected by aircraft operations, viewing geometry that varies
352 systematically along the flight path resulting in amplitude artifacts amplified by landform and
353 landcover heterogeneity. Even after separating homogeneous grassland pixels, there is
354 contamination from multiple bounce artifacts at grassland-forest transitions and adjacent wetlands
355 that cannot be resolved at 30 or 60 m resolution. Other errors embedded in the retrieval are



356 associated with downscaling of HRRR forcings that produce biased snow priors, snow hydrology
 357 model assumptions, and errors tied to the background backscatter estimation. Combined these
 358 errors can lead to weak convergence of the Bayesian optimization algorithm resulting in large
 359 backscatter residuals. To account for these errors, SnowSAR pixels for which the relative residual
 360 backscatter (RRB) between Base-AM simulated σ_{total} and SnowSAR measurements was greater
 361 than 30% were identified as unsuccessful. In an operational context, these pixels would be flagged
 362 and identified as failed or highly uncertain retrievals. The successful retrieval fraction after
 363 restricting the range of incidence angles and imposing the $\text{RRB} < 30\%$ criterion is summarized in
 364 Table 4 for the four flights, and 1|2 layer snowpack retrievals at 30 and 90 m resolution. Except
 365 for the later flight path over the predominantly forested areas in the eastern sector of Grand Mesa
 366 (Fig.1), the fraction of successful retrievals by restricting the incidence angle and RRB varies
 367 between 75 and 87% across the four SnowSAR flights with a maximum absolute bias of 1.2 dB.

368

369 **Table 4:** Spatial bias between SnowSAR backscatter and converged backscatter from Base-AM for successful retrievals for
 370 grassland pixels at 30 and 90 m spatial resolution over each flight. Successful retrievals are for pixels with local incidence angles
 371 in the 30° - 45° range and relative residual backscatter (RRB) of less than 30% for each of the four flights. Shaded columns are for
 372 retrievals at 90 m resolution.

373

Flight Time	Successful Retrieval Fraction				Bias (Observed - Converged) [dB]							
	1 Layer		2 Layer		1 Layer				2 Layer			
	30 m	90 m	30 m	90 m	30 m		90 m		30 m		90 m	
					X	Ku	X	Ku	X	Ku	X	Ku
18:11:38	0.86	0.87	0.85	0.86	0.92	-0.45	0.96	-0.48	0.94	-0.46	0.97	-0.50
18:43:20	0.75	0.75	0.75	0.75	1.08	-0.54	0.98	-0.36	1.07	-0.46	0.98	-0.37
18:59:02	0.78	0.81	0.81	0.81	1.20	-0.78	1.21	-0.79	1.15	-0.73	1.22	-0.83
20:23:38	0.66	0.69	0.57	0.69	0.51	-0.58	0.70	-0.43	0.62	-0.85	0.72	-0.45

374

375

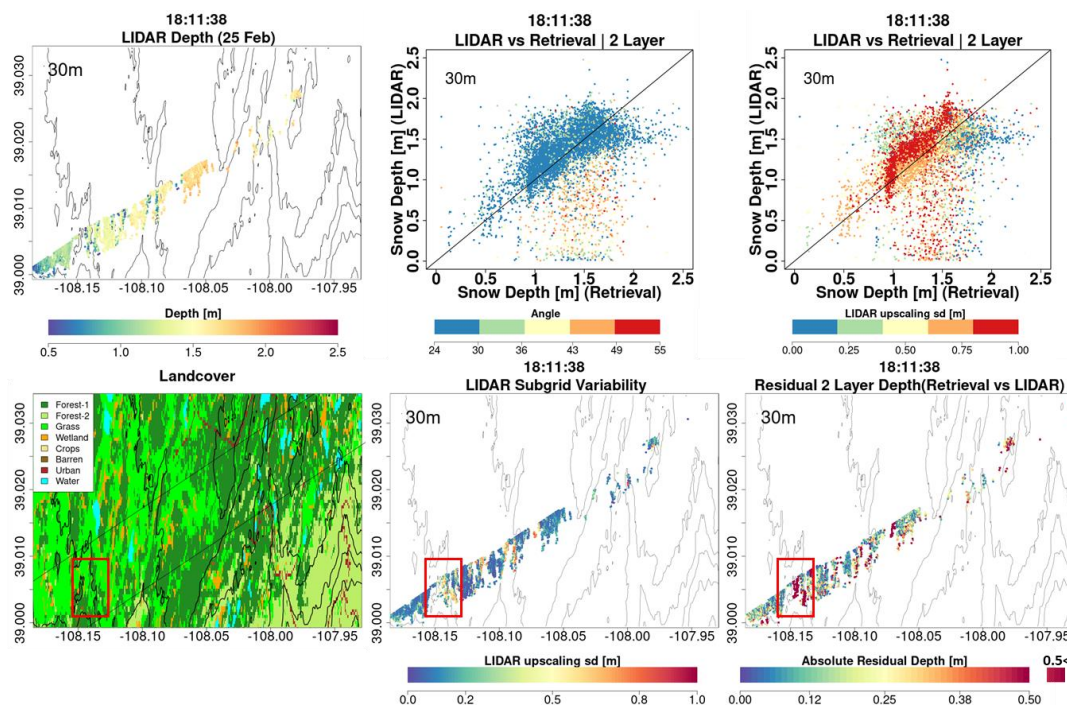
376 5.2. Retrieval Skill

377 Figure 7 compares LIDAR snow depth (Fig. 7a) against colocated SnowSAR retrievals at 30 m
 378 for the SNOWSAR flight at 18:11:38 GMT (GMT=MST+6). The SnowSAR retrievals for high
 379 incidence angles underestimate the LIDAR snow depth (orange and red points). Lemmetyinen et
 380 al. (2022) suggested a nominal incidence angle of 35° - 45° for retrievals ensuring proper focusing
 381 and calibration of SnowSAR swaths. CB22 showed good skill in forward backscatter simulations
 382 for incidence angles as low as 30° . Overall the retrievals here also show very good performance
 383 for incidence angles between 30° - 45° . Note however the large residuals for SnowSAR retrievals
 384 with high incidence angles (red and orange points in Fig. 7b) corresponding to LIDAR pixels with
 385 shallow snow depth (below the 1:1 line) and large subgrid-scale variability (orange and red points,
 386 Fig. 7c). Analysis for all flights at both 30 and 90 m resolution can be found in Appendix A (
 387 please see Figs. A1 and A2 similar to Fig. 7b; and Figs. A3 and A4 similar to Fig. 7c). Figures
 388 7d, 7e, and 7f show the landcover, spatial distribution of subgrid standard deviation and absolute



389 residual (Retrieved – LIDAR) snow depth for the same flight. Along the edges of forest, the
 390 standard deviation in the upscaled pixels is large due to high heterogeneity that cannot be resolved
 391 by the the LIDAR fusion algorithm for snow depth retrieval (Painter et al. 2016). The red box
 392 identifies an area with complex grassland-forest boundaries (Fig. 7d) and high subgrid scale
 393 variability (Fig. 7e) resulting in poor LIDAR estimates. The edge of wetlands also has
 394 comparatively higher residuals than completely homogeneous grasslands. This corresponds to the
 395 LIDAR pixels with standard deviation of more than 0.3 m (yellow, orange and red in Fig. 7c).
 396 Therefore, only LIDAR pixels with subgrid-scale standard deviations $\leq 0.3\text{m}$ are used for
 397 assessment of retrievals.

398



399

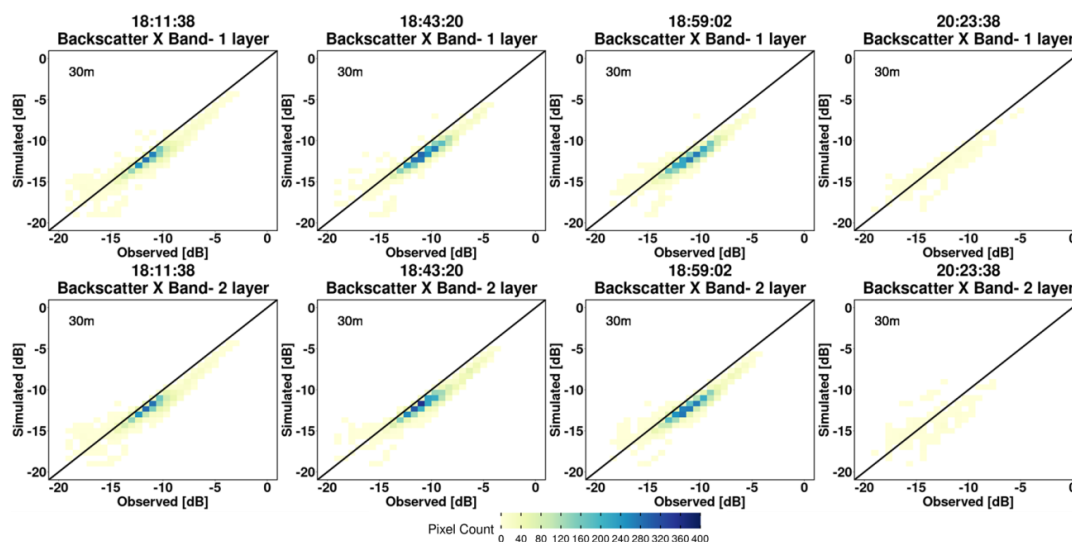
400 **Figure 7:** a) Snow depth measurements using airborne LIDAR on 2/25/17, 4 days after the SnowSAR flights. b) Comparison
 401 between LIDAR snow depth and the retrieved snow depth for 2-layer snowpack for the SnowSAR on 2/21/17 at 18:11:38 GMT.
 402 The pixels are color-coded according to the incidence angle for the SnowSAR observations. c) The same comparison is shown;
 403 however, the pixels are color-coded according to the subgrid-scale variability of LIDAR snow depth within the corresponding 30
 404 m pixel. Pixels on the edge of forests and grassland have higher standard deviations. d) Landcover distribution along the flight
 405 path. e) Spatial distribution of subgrid-scale variability of upscaled LIDAR snow depth at 30m corresponding to part c). The edges
 406 of forests have higher subgrid-scale variability due to errors in the LIDAR snow depth retrievals at high resolution. f) Absolute
 407 residual between retrieved and LIDAR snow depth. Residuals equal to 0.5 m and above are grouped in the same category. The red
 408 box in the parts d), e), and f) delineates an area with large absolute residuals. The areas on the edge of the forests have large subgrid-
 409 scale variability in the LIDAR retrievals contributing and there are vegetation-snowpack backscatter interactions that are not
 410 accounted for in the retrievals. Additionally, areas surrounding the wetlands have comparatively higher residuals than the
 411 homogenous grasslands.

412



413 Figures 8 and 9 show heatmaps to compare successful retrievals and observed X-band and Ku-
414 band VV-pol total backscatter at 30 m resolution. There is good agreement between the two values
415 for both the bands specially for -15 dB to -10 dB without significant differences between single
416 and two-layer snowpack retrievals. There is a constant positive bias in case of X-band simulations
417 compared to observations, whereas Ku-band has a constant negative bias as quantified in Table 4.
418 Overall, the retrievals at 90 m resolution show better agreement than those at 30 m resolution due
419 to averaging (Figs. A5 and A6).

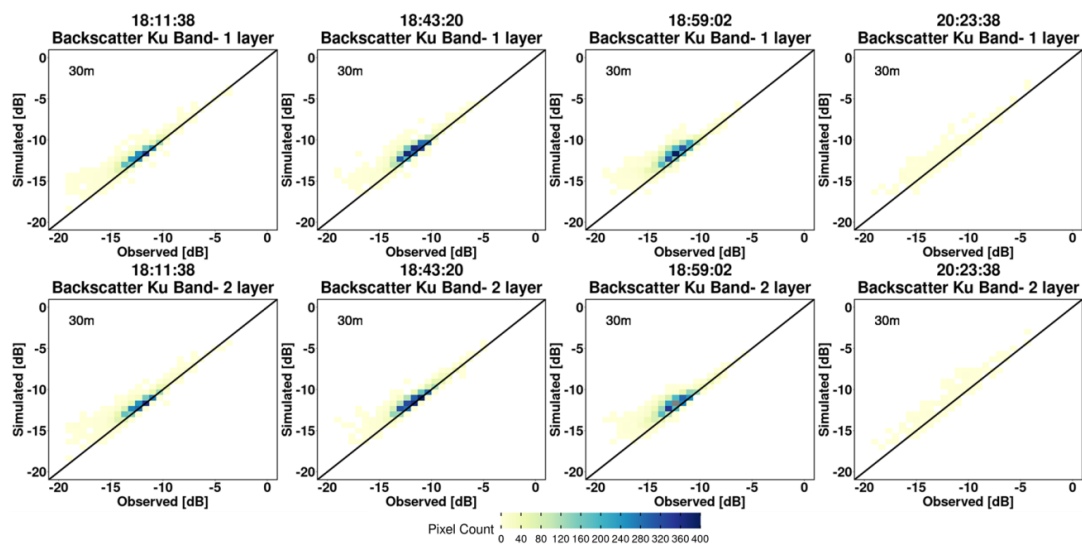
420



421

422 **Figure 8:** Heatmaps of SnowSAR (observed) backscatter (X-band) versus converged (simulated) backscatter at 30 m resolution:
423 1-layer snowpack (top row); 2-layer snowpack (bottom row). Successful retrievals are for pixels with local incidence angles in the
424 30°- 45° range and relative residual backscatter (RRB) of less than 30% for each of the four flights (see Table 4).

425



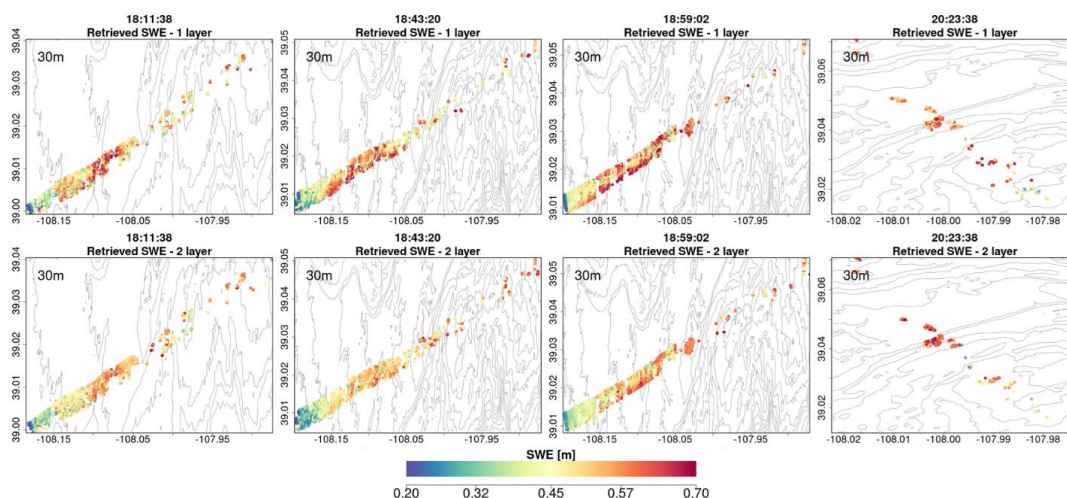
426

427 **Figure 9:** Heatmaps of SnowSAR (observed) backscatter (Ku-band) versus converged backscatter (simulated) for successful
428 retrievals at 30 m resolution: 1-layer snowpack (top row) and 2-layer snowpack (bottom row). Successful retrievals are for pixels
429 with local incidence angles in the 30°- 45° range and relative residual backscatter (RRB) of less than 30% for each of the four
430 flights (see Table 4).

431

432 Maps of successful SWE retrievals for the four SnowSAR flight paths are shown in Fig. 10 and
433 Fig. A7 at 30 m and 90 m resolution, respectively. The retrievals capture well the west-east
434 gradient in SWE, and show realistic spatial variability across Grand Mesa. The very low SWE and
435 shallower snow depths at the easternmost boundary of the flightlines are underestimates
436 introduced by upscaling of the SNOWSAR backscatter values where there are significant changes
437 in topography at the edge of the Plateau (see Fig.2).

438



439

440 **Figure 10:** Spatial distribution of successful SWE retrievals for 1-layer and 2-layer snowpacks in grassland pixels at 30 m
441 resolution. Successful retrievals are for pixels with local incidence angles in the 30°- 45° range and relative residual backscatter
442 (RRB) of less than 30% for each of the four flights (see Table 4).

443

444 Heatmaps of total snow depth priors (MSHM predicted snow depth) against LIDAR snow depth
445 are shown in Fig. 11 and Figs. A8 at 30 m and 90 m resolution and can be contrasted with heatmaps
446 of total snow depth posteriors) against LIDAR snow depth in Figs. 12 and 13 using both single
447 and two-layer retrievals. Note the narrow range of the prior snow depths concentrated around 1.5
448 m and the positive bias relative to LIDAR. The posteriors show much wider range of variability
449 and deeper snow consistent with the LIDAR data for both single and two-layer retrievals, albeit
450 with better agreement for the latter with high counts overlaying the 1:1 line at both spatial
451 resolutions. This behavior is further confirmed by examining the snow depth histograms in Figs.
452 A9 and A10 at 30 m and 90m resolution. The retrievals capture well the range of the LIDAR snow
453 depths for all flights, and there is a substantial improvement in the shape of the distributions as
454 revealed by the heatmaps.

455

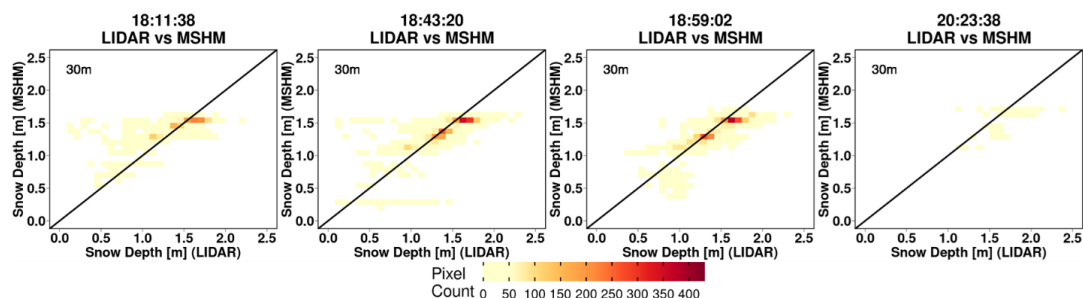
456

457

458

459

460



461

462 **Figure 11:** Heatmap of LIDAR and MSHM predicted snow depth priors at 30 m resolution using overlapping pixels from the
463 MSHM and LIDAR. Only pixels with incidence angle between 30° -45°, and moderate sub-grid scale variability of LIDAR snow
464 depth (< 0.3).

465

466 Quantitative assessment metrics are presented in Tables 5 and 6 for the comparison between
467 various snow depth datasets at 30 and 90 m resolutions, respectively. The snow depth MARE is
468 higher for the retrievals compared to the priors (MSHM) due to the fact that MARE is an effective
469 metric capturing distance from the mean. CB20 showed that the MSHM simulated average snow
470 mass accumulation at the Grand Mesa scale is within 10% of observations at a monthly time-scale
471 in February 2017. The BC coefficients show significant agreement between in the shapes of the
472 distributions at 0.95 or above at 30m resolution using the two-layer retrievals for the west-east
473 flights, and 0.76 for the fourth flight over the forest area at 20:23:38 GMT. There is significant
474 improvement in the statistical similarity of the snow depth retrievals vis-à-vis the LIDAR data for
475 all cases, and more so for the fourth flight. In all cases 30 m retrievals and two-layer retrievals
476 performed better than 90 m and single-layer retrievals for snow depth. This is explained in part
477 by landcover classification errors that are smaller at 30 m. Figure A11 shows that the number of
478 pixels where retrievals produce large mean absolute residuals is very small and characterize by
479 low confidence in the LIDAR estimates.

480

481

482

483

484

485

486

487

488

489

490

491



492 **Table 5:** Summary of statistics and error metrics of the 3 snow depth (SD) data sets at 30 m resolution: LIDAR measurements,
 493 MSHM predictions, and successful SnowSAR retrievals for grassland pixels and subgrid-scale standard deviation (σ) of less than
 494 0.3 m for the upscaled LIDAR pixel. MARE – Mean Absolute Relative Error (Eq. 6); BC – Bhattacharya Coefficient (Eq. 7). Here
 495 mean and standard deviation refer to the spatial distribution, unlike the prior mean and standard deviation used in Base-AM (Table
 496 3). Successful retrievals are for pixels with local incidence angles in the 30°- 45° range and relative residual backscatter (RRB) of
 497 less than 30% for each of the four flights (see Table 4).

Flight (GMT)	N Layer	Spatial SD μ [m]			Spatial SD σ [m]			MARE SD		BC SD	
		Retrieved	MSHM	LIDAR	Retrieved	MSHM	LIDAR	Retrieved-LIDAR	MSHM-LIDAR	Retrieved-LIDAR	MSHM-LIDAR
18:11:38	1	1.39	1.42	1.42	0.32	0.15	0.28	0.19	0.11	0.94	0.67
18:43:20		1.41	1.38	1.42	0.32	0.21	0.27	0.18	0.11	0.96	0.75
18:59:02		1.49	1.38	1.44	0.33	0.20	0.27	0.18	0.09	0.94	0.76
20:23:38		1.66	1.58	1.77	0.36	0.16	0.22	0.21	0.13	0.71	0.25
18:11:38	2	1.38	1.41	1.40	0.30	0.17	0.29	0.14	0.12	0.98	0.67
18:43:20		1.35	1.38	1.42	0.31	0.20	0.28	0.14	0.11	0.97	0.75
18:59:02		1.40	1.38	1.44	0.31	0.20	0.27	0.12	0.09	0.95	0.75
20:23:38		1.89	1.61	1.80	0.39	0.14	0.24	0.17	0.12	0.76	0.23

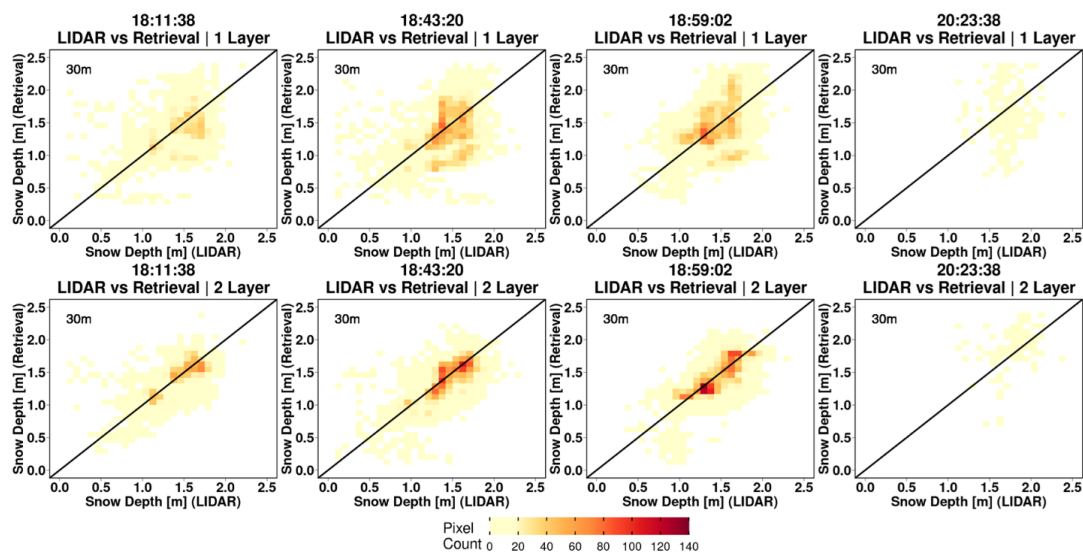
498

499 **Table 6 -** Summary of statistics and error metrics of the 3 snow depth (SD) data sets at 90 m resolution: LIDAR measurements,
 500 MSHM predictions, and successful SnowSAR retrievals for grassland pixels and subgrid-scale standard deviation (σ) of less than
 501 0.3 m for the upscaled LIDAR pixel. MARE – Mean Absolute Relative Error; BC – Bhattacharya Coefficient. Here mean and
 502 standard deviation refer to the spatial distribution, unlike the Prior mean and standard deviation used in Base-AM. Successful
 503 retrievals are for pixels with local incidence angles in the 30°-45° range and relative residual backscatter (RRB) of less than 30%
 504 for each of the four flights (see Table 4).

Flight (GMT)	N Layer	Spatial SD μ [m]			Spatial SD σ [m]			MARE SD		BC SD	
		Retrieved	MSHM	LIDAR	Retrieved	MSHM	LIDAR	Retrieved-LIDAR	MSHM-LIDAR	Retrieved-LIDAR	MSHM-LIDAR
18:11:38	1	1.41	1.42	1.40	0.33	0.18	0.26	0.19	0.09	0.90	0.78
18:43:20		1.27	1.39	1.41	0.32	0.19	0.25	0.21	0.08	0.90	0.85
18:59:02		1.48	1.38	1.42	0.37	0.20	0.25	0.21	0.07	0.90	0.82
20:23:38		1.68	1.52	1.66	0.38	0.17	0.19	0.24	0.12	0.66	0.50
18:11:38	2	1.41	1.42	1.40	0.35	0.18	0.26	0.15	0.09	0.95	0.77
18:43:20		1.29	1.39	1.41	0.32	0.19	0.25	0.16	0.08	0.92	0.85
18:59:02		1.41	1.38	1.42	0.35	0.20	0.25	0.15	0.07	0.92	0.82
20:23:38		1.67	1.52	1.66	0.45	0.17	0.19	0.22	0.12	0.76	0.50

505

506



507

508 **Figure 12:** Heatmap of LIDAR versus successful snow depth retrievals at 30 m resolution using overlapping LIDAR and retrieval
509 pixels. Successful retrievals are for pixels with local SnowSAR incidence angles in the 30°- 45° range and relative residual
510 backscatter (RRB) of less than 30% for each of the four flights (see Table 4). LIDAR SD in pixels with subgrid scale variability
511 corresponding to standard deviation of less than 0.3 m for the upscaled 90 m LIDAR pixel are not included.

512

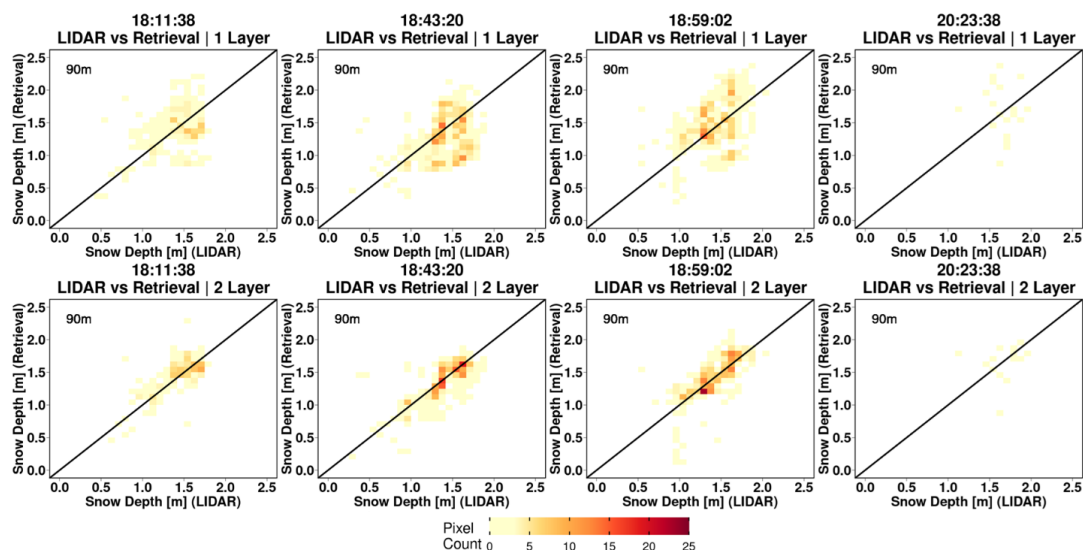
513

514

515

516

517



518

519 **Figure 13:** Heatmaps of LIDAR versus successful snow depth retrievals at 90 m resolution using overlapping LIDAR and retrieval
520 pixels. Successful retrievals are for pixels with local SnowSAR incidence angles in the 30°- 45° range and relative residual
521 backscatter (RRB) of less than 30% for each of the four flights (see Table 4). LIDAR SD in pixels with subgrid scale variability
522 corresponding to standard deviation of less than 0.3 m for the upscaled 90 m LIDAR pixel are not included.

523

524 Composite spatial maps of successful SWE retrievals from all flights overlain by the snowpit
525 measurements between 20-24 February are shown in Fig. 14. Note the consistency at 30 m and 90
526 m resolutions as well as the overall agreement between SWE at snowpits and SWE retrievals on
527 the flightlines. Tables 7 and 8 summarize the average absolute relative errors between snowpits
528 and all SWE retrievals within 100 m of the snowpits. The results are significantly better for two-
529 layer snowpack retrievals. The mean absolute relative errors at 30 m resolution are 0.22 and 0.13
530 for 1 layer and 2 layer snowpacks respectively. The mean absolute relative errors at 90 m resolution
531 are 0.2 and 0.12 for 1 layer and 2 layer snowpacks respectively. There is a variable number of
532 pixels for each snow pit, which in the case of 51S is so small that indicates it is not in the flight
533 path. After removing snowpits in the central area marked in Fig. A12 is due to very heterogeneous
534 landcover including water, forest, (4500) and proximity to roads (53W and 44E), the average
535 absolute relative SWE residuals is 5-7% (15-18%) for the two-layer (single-layer) retrieval
536 algorithm.

537

538

539

540

541

542



543

544

545 **Table 7:** Evaluation of successful SWE retrievals at 30 m resolution against SWE at SnowEx'17 snow pits and
 546 retrieved snowpacks at 30 m resolution. All N pixels with centroids within 100 m of each snow pit are in the Grasslands
 547 (according to the Landcover dataset at 30 m resolution, see Table 1). SD – snow depth. Shaded rows correspond to
 548 large local MARE (Mean Absolute Relative Error, Eq. 6).

Date	x	y	Pit SD (m)	Pit SWE (m)	Retrieved SWE (m)		MARE		N pixels	Avg. Dist (m)	Pit ID
					1 Lyr	2 Lyr	1 Lyr	2 Lyr			
2/20/2017	-108.184	39.014	1.15	0.368	0.455	0.386	0.236	0.049	28	18	KC1C
2/20/2017	-108.184	39.014	1.19	0.386	0.457	0.387	0.184	0.003	27	12	KC1E
2/20/2017	-108.184	39.014	1.18	0.386	0.456	0.387	0.181	0.003	26	15	KC1N
2/20/2017	-108.184	39.013	1.24	0.414	0.456	0.387	0.101	0.065	27	20	KC1S
2/20/2017	-108.184	39.014	1.30	0.435	0.455	0.385	0.046	0.115	29	11	KC1W
2/22/2017	-108.136	39.006	1.32	0.436	0.556	0.484	0.275	0.110	22	8	29E
2/22/2017	-108.090	39.021	1.65	0.583	0.685	0.596	0.175	0.022	19	17	38E
2/22/2017	-108.060	39.030	2.10	0.763	0.368	0.449	0.518	0.412	12	16	53W
2/22/2017	-108.044	39.017	1.68	0.566	0.480	0.505	0.152	0.108	5	51	63E
2/22/2017	-108.049	39.017	1.49	0.48	0.494	0.513	0.029	0.069	13	29	63W
2/22/2017	-108.029	39.032	1.66	0.55	0.558	0.581	0.015	0.056	18	15	67N
2/23/2017	-108.067	39.029	2.13	0.761	0.593	0.504	0.221	0.338	9	23	44E
2/23/2017	-108.061	39.030	1.59	0.568	0.365	0.408	0.357	0.282	3	75	51S
2/24/2017	-108.033	39.030	1.80	0.576	0.657	0.573	0.141	0.005	20	10	0
2/24/2017	-108.033	39.030	1.84	0.598	0.652	0.581	0.090	0.028	21	14	800
2/24/2017	-108.033	39.030	1.80	0.571	0.650	0.581	0.138	0.018	22	19	1390
2/24/2017	-108.033	39.030	1.75	0.566	0.654	0.581	0.155	0.027	21	15	2000
2/24/2017	-108.033	39.030	1.67	0.560	0.654	0.581	0.168	0.037	21	9	2500
2/24/2017	-108.034	39.030	1.12	0.331	0.660	0.580	0.994	0.752	18	19	4500

549

550

551

552

553

554

555

556

557

558

559

560

561



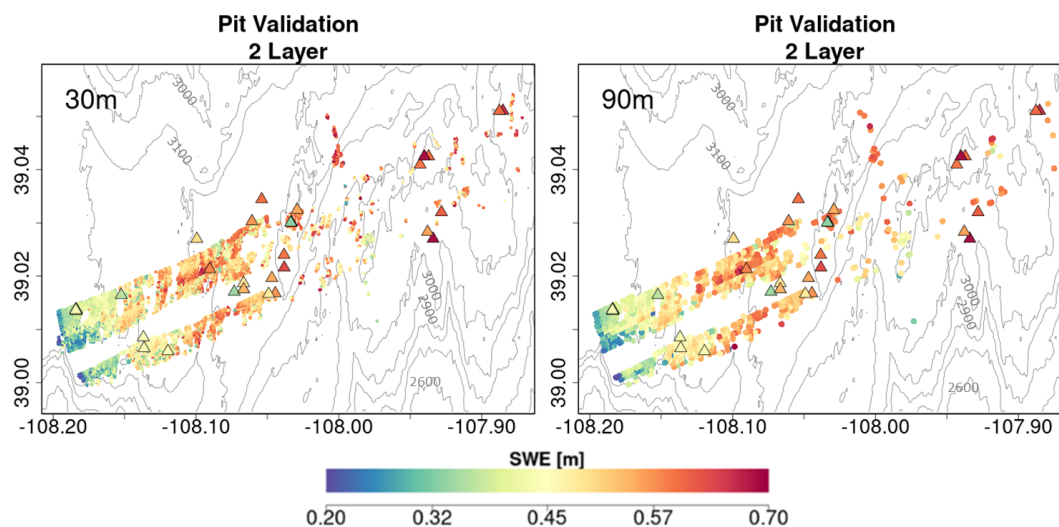
562

563

564 **Table 8:** Evaluation of successful SWE retrievals at 90 m resolution against SWE at SnowEx'17 snow pits and
 565 retrieved snowpacks at 90 m resolution. All N pixels with centroids within 100 m of each snow pit are in the
 566 Grasslands (according to the Landcover dataset at 90 m resolution, see Table 1). SD – Snow depth. Rows in italics
 567 correspond to large local MARE (Mean Absolute Relative Error, Eq. 6).

Date	x	y	Pit SD (m)	Pit SWE (m)	Retrieved SWE (m)		Mean Abs Rel Error		N pixels	Avg. Dist (m)	Pit ID
					1 Lyr	2 Lyr	1 Lyr	2 Lyr			
2/20/2017	-108.184	39.014	1.15	0.368	0.473	0.398	0.29	0.08	4	18	KC1C
2/20/2017	-108.184	39.014	1.19	0.386	0.471	0.397	0.22	0.03	3	12	KC1E
2/20/2017	-108.184	39.014	1.18	0.386	0.473	0.399	0.22	0.03	2	29	KC1N
2/20/2017	-108.184	39.013	1.24	0.414	0.474	0.398	0.15	0.04	3	27	KC1S
2/20/2017	-108.184	39.014	1.3	0.435	0.476	0.399	0.09	0.08	3	47	KC1W
2/22/2017	-108.136	39.006	1.32	0.436	0.572	0.490	0.31	0.12	2	39	29E
2/22/2017	<i>-108.060</i>	<i>39.030</i>	<i>2.10</i>	<i>0.763</i>	<i>0.340</i>	<i>0.384</i>	<i>0.55</i>	<i>0.50</i>	<i>1</i>	43	53W
2/22/2017	-108.044	39.017	1.68	0.566	0.454	0.499	0.20	0.12	1	75	63E
2/22/2017	-108.049	39.017	1.49	0.480	0.521	0.530	0.09	0.10	1	29	63W
2/22/2017	-108.029	39.032	1.66	0.550	0.529	0.553	0.04	0.01	4	47	67N
2/23/2017	-108.067	39.029	2.13	0.761	0.751	0.606	0.01	0.20	1	70	44E
2/24/2017	-108.033	39.030	1.8	0.576	0.718	0.601	0.25	0.04	3	60	0
2/24/2017	-108.033	39.030	1.84	0.598	0.717	0.600	0.20	0.00	2	57	800
2/24/2017	-108.033	39.030	1.80	0.571	0.717	0.600	0.26	0.05	2	55	1390
2/24/2017	-108.033	39.030	1.75	0.566	0.687	0.592	0.21	0.05	1	54	2000
2/24/2017	-108.033	39.030	1.67	0.560	0.687	0.592	0.23	0.06	1	54	2500
2/24/2017	<i>-108.034</i>	<i>39.030</i>	<i>1.12</i>	<i>0.331</i>	<i>0.687</i>	<i>0.592</i>	<i>1.08</i>	<i>0.79</i>	<i>1</i>	62	4500
2/20/2017	-108.184	39.014	1.15	0.368	0.473	0.398	0.29	0.08	4	18	KC1C
2/20/2017	-108.184	39.014	1.19	0.386	0.471	0.397	0.22	0.03	3	12	KC1E

568



569



570 **Figure 14:** Composite spatial distribution of SWE (2-layer snowpack) successfully retrieved at 30m (left) and 90m (right)
571 resolution for grassland pixels for the four SnowSAR flights. Snow pits (19-24 Feb, Fig. 4, Tables 7 and 8) are marked by triangles
572 colored according to SWE. SnowEx'17 snow pit locations are marked by triangles and colored according to SWE. Successful
573 retrievals are for pixels with local incidence angles in the 30°- 45° range and relative residual backscatter (RRB) of less than 30%
574 for each of the four flights (see Table 4). Gray elevation contours are plotted every 100m.

575

576 **6. Conclusion**

577 A Bayesian physical-statistical SWE retrieval framework leveraging prior work (CB20, CB22,
578 P17, P23, Fig. 5) was applied to airborne X- and Ku-band measurements yielding robust results
579 for multiple flights including overlapping paths over grassland and mixed grassland and forest in
580 Grand Mesa, Colorado. Prior distributions of snowpack parameters were obtained from a
581 multilayer snow hydrology model with atmospheric forcing derived from operational NWP
582 forecasts and analysis (CB20, CB22). In order to reconcile the number of independent
583 measurements, physical constraints, and reduce the number of snowpack parameters, snowpack
584 stratigraphy was mapped into single-layer and two-layer snowpacks for Bayesian inference using
585 Base-AM (P17, P23). The SnowSAR measurements were averaged to 30 and 90 m resolutions,
586 and retrievals were conducted for every measurement pixel along the flight lines. Retrievals for
587 measurements with convergence backscatter relative errors less than 30% ($\pm 1.2\text{dB}$) and for
588 incidence angles in the 30°-45° range were considered successful over grasslands, corresponding
589 to 75-87% of all retrievals.

590 The retrievals (i.e. the local mean of the posterior distribution) were evaluated against the spatial
591 distribution of LIDAR snow depth estimates up to 2 m and against snowpit SWE measurements
592 up to 700 mm. Note that the LIDAR and snowpit measurements are not at the same time of the
593 SnowSAR flights, and the assessment of retrieval skill was conducted over a period of five days
594 without snowfall or significant day-to-day weather changes. The two-layer snowpack retrievals
595 perform better overall being able to capture the statistical variability of snow depth with high
596 fidelity, with SWE relative errors $\leq 7\%$ as compared with 18% for single-layer SWE retrievals,
597 and snow depth absolute retrieval residuals 10-20% depending on landcover heterogeneity and
598 measurement uncertainty. The statistical structure of retrieved snow depth is similar to that
599 estimated by LIDAR, which is indicative of the retrievals ability to capture snow patterns and
600 scaling behavior to support process studies. For satellite-based monitoring from space in the
601 context of a future snow mission, time-series of measurements would be available that should
602 improve the estimates of the priors for the present retrieval cycle. This is not possible for field
603 experiments such as SnowEx'17, and thus improved results would be expected under realistic
604 satellite-based applications. NWP forecasts are available worldwide and therefore this retrieval
605 framework can be applied to SAR measurements anywhere.

606 The radar model used in this study (MEMLS) does incorporate snow-ground-vegetation scattering
607 interactions. Grassland vegetation during the accumulation season is assumed to be submerged
608 and the impact of vegetation is included in the estimation of the background backscatter (σ_{bkg} , Fig.
609 1). Because the landcover data are categorical, in addition to the uncertainty of the data at 30 m
610 resolution, additional uncertainty is tied to the selection of homogeneous grassland pixels at 90
611 resolution, which explains some of the unsuccessful retrievals especially along the grassland-forest



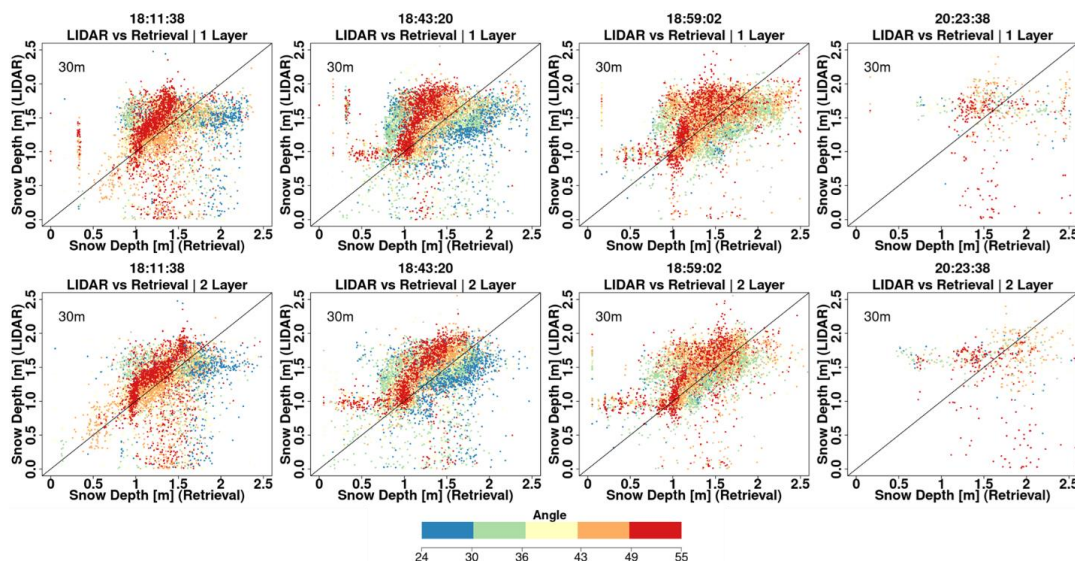
612 and shrub boundaries. The potential for estimating σ_{bkg} independently for each location as
613 proposed by Cao and Barros (2023) provides an alternative to simplify the retrieval workflow and
614 target the Bayesian inference to the snowmass and volume backscatter ($\sigma_{\text{vol}} = \sigma_{\text{total}} - \sigma_{\text{bkg}}$).

615 Airborne measurements are characterized by large changes in viewing geometry across the flight-
616 line and due to other factors such as variable winds and turbulence depending on weather
617 conditions, thus pointing to improved skill from satellite platforms. Building on previous mission
618 concepts (e.g. Rott et al. 2012) and leveraging substantial theory advances and field campaigns in
619 the last decade, this study demonstrates the utility and effectiveness of X- and Ku-band SAR
620 technology to remotely monitor snowmass at high spatial resolution and with accuracy and
621 uncertainty that meet the requirements expressed in the most recent Earth Science and Applications
622 from Space Decadal Survey (NASEM, 2018).

623

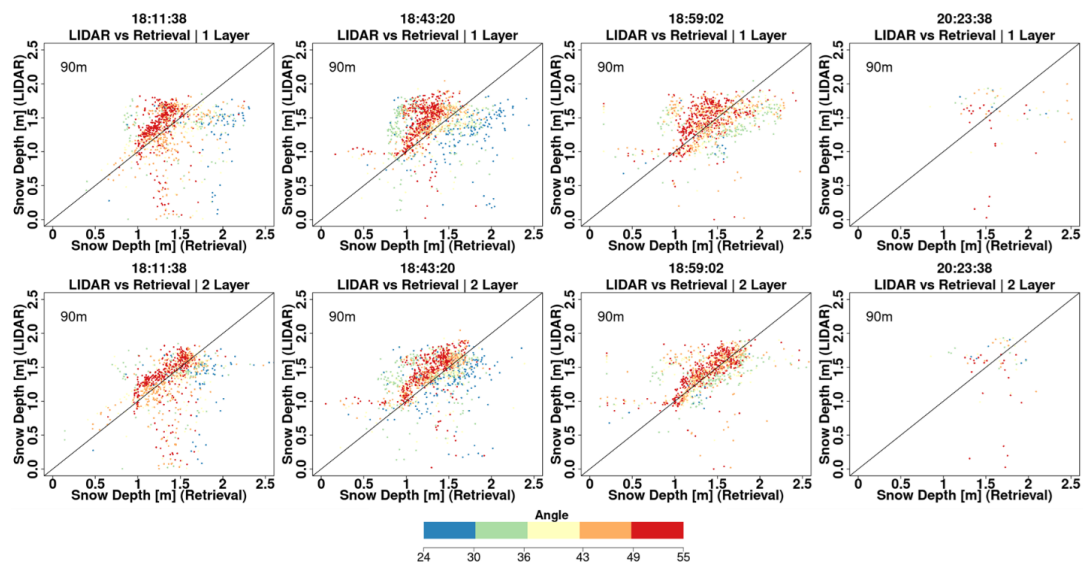
624 7. Appendix A

625



626

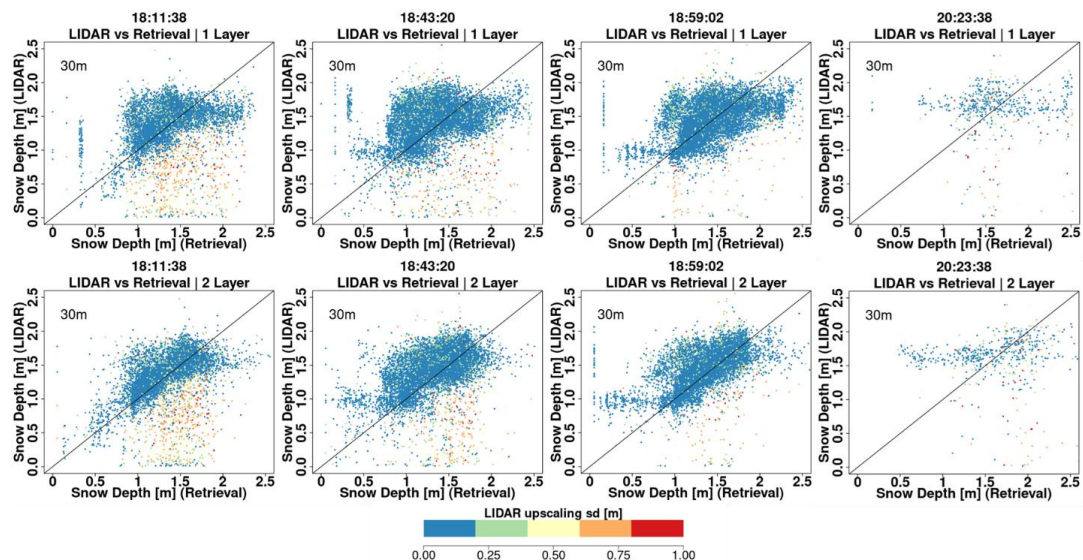
627 **Figure A1:** Same as Fig. 7b with pixels color coded according to the local SnowSAR incidence angle for all four flightlines and
628 for single-(top row) and two-layer (bottom row) retrievals at 30 m resolution.



629

630 **Figure A2:** Same as Fig. 7b with pixels color coded according to the local SnowSAR incidence angle for all four flightlines and
 631 for single-(top row) and two-layer (bottom row) retrievals at 90 m resolution.

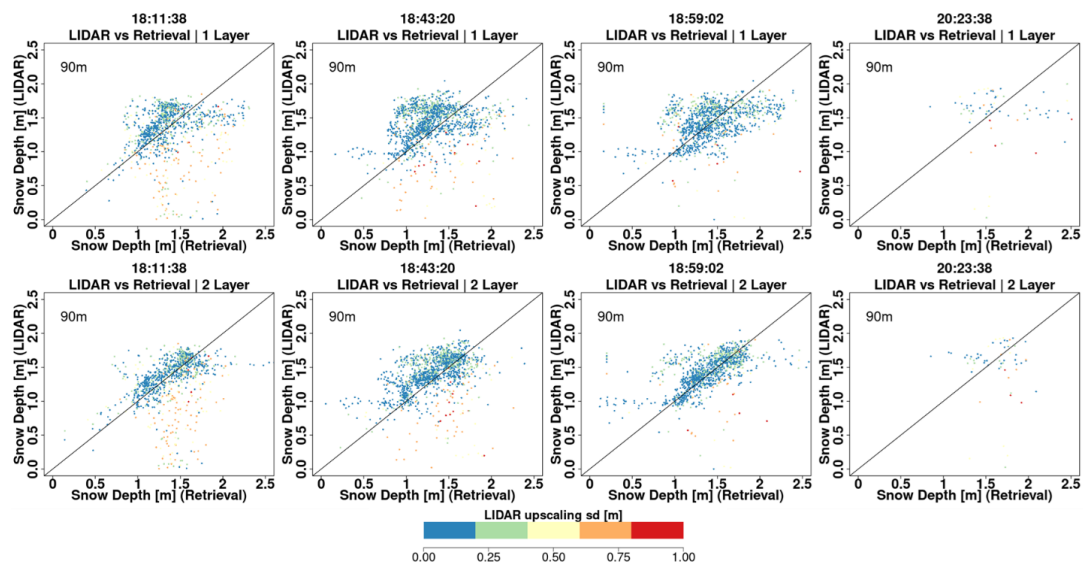
632



633

634 **Figure A3:** Comparison between LIDAR snow depth and successful retrievals for single and two-layer algorithms. The pixels are
 635 color coded according to the subgrid scale variability of the 30 m upscaled LIDAR pixel.

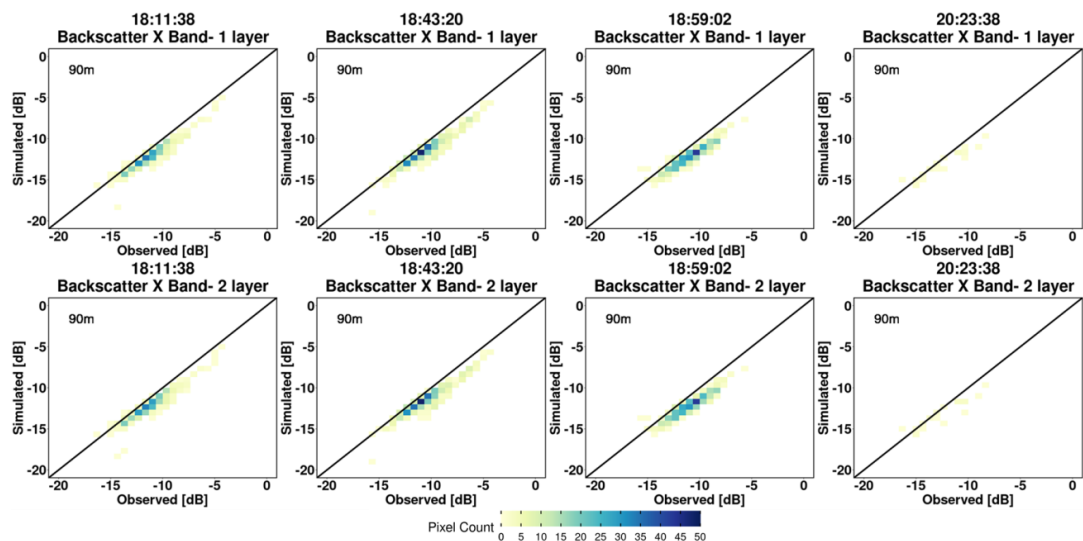
636



637

638 **Figure A4:** Comparison between SnowSAR snow depth and successful retrievals. The pixels are color coded according to the
 639 subgrid scale variability of the 90 m upscaled LIDAR pixel.

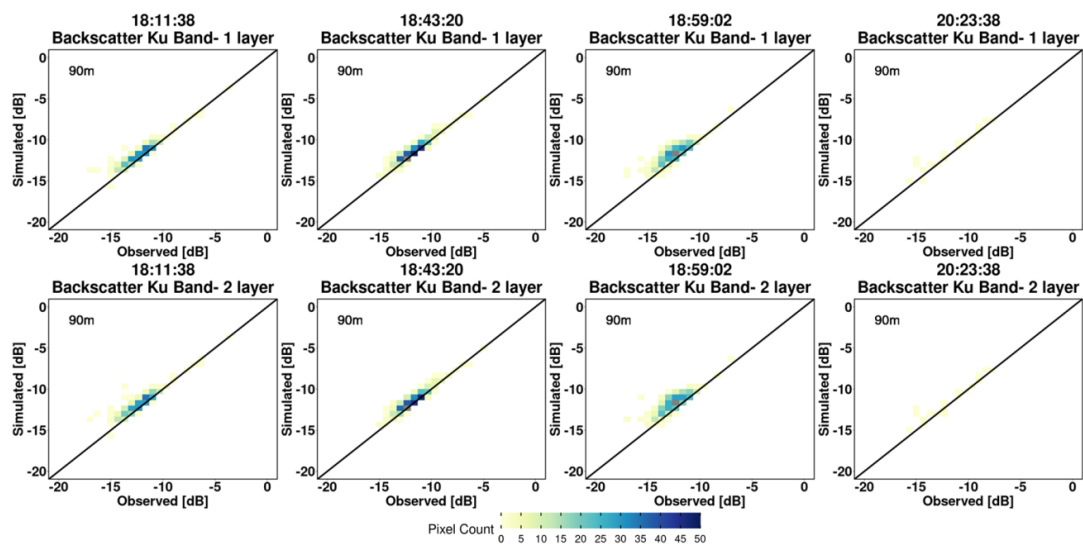
640



641

642 **Figure A5:** Comparison between SnowSAR backscatter (X-band) and BASE-AM converged backscatter at 90 m resolution for
 643 successful retrievals. Error statistics can be found in Table 4.

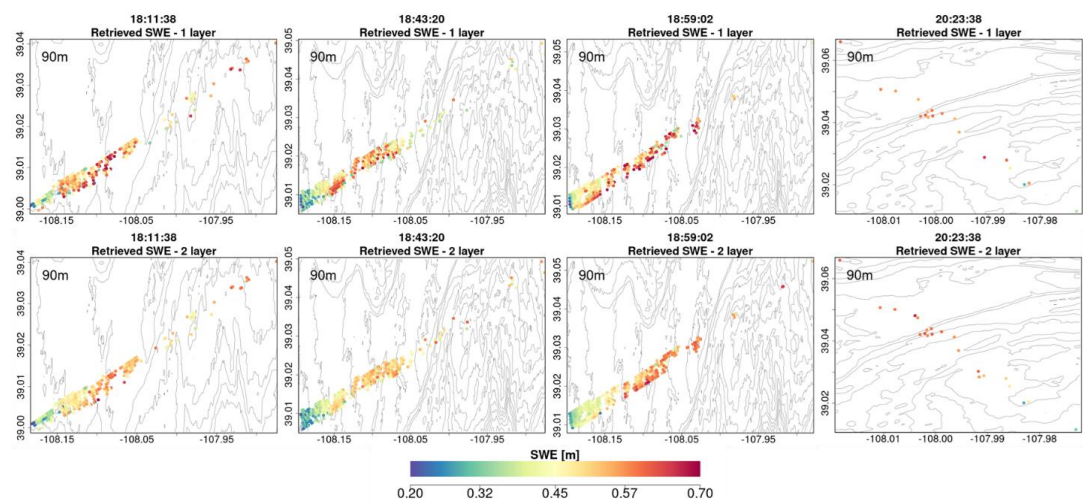
644



645

646 **Figure A6** - Comparison between SnowSAR backscatter (Ku-band) and Base-AM converged backscatter at 90 m resolution for
647 successful retrievals. Error statistics can be found in Table 4.

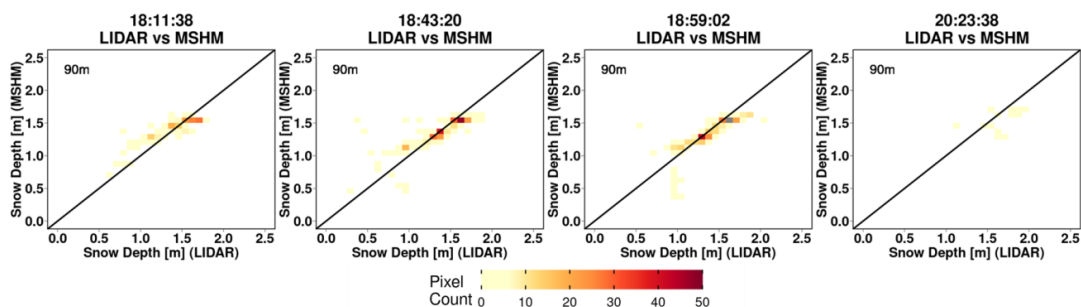
648



649

650 **Figure A7:** Spatial distribution of successful SWE retrievals for single- and 2-layer snowpacks at 90 m resolution. The retrievals
651 are for grassland pixels only.

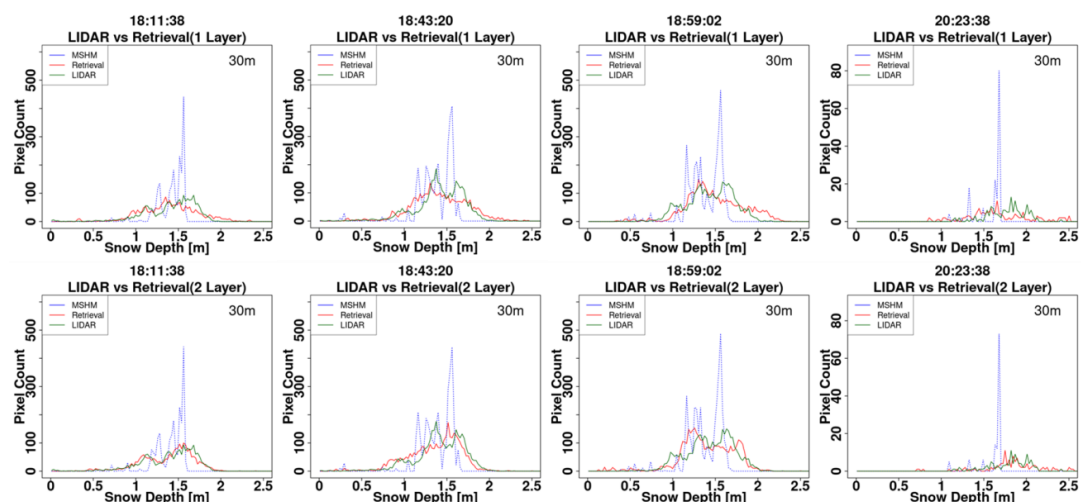
652



653

654 **Figure A8:** Heatmaps of LIDAR snow depth and snow depth predicted by MSHM at the time of SnowSAR flights for
 655 overlapping pixels at 90 m resolution.

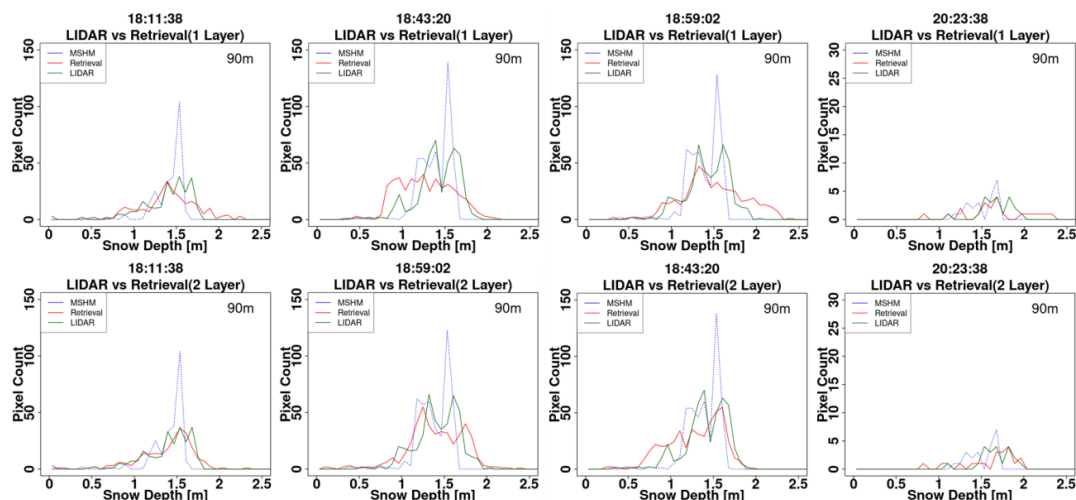
656



657

658 **Figure A9:** Histogram of snow depth (SD) from LIDAR, MSHM, and successful retrievals at 30 m using 1- and 2- layer
 659 snowpacks. The total number of pixels for each snow depth product is the same. Successful retrievals are for pixels with local
 660 incidence angles in the 30°- 45° range and relative residual backscatter (RRB) of less than 30% for each of the four flights (see
 661 Table 4). LIDAR SD in pixels with subgrid scale variability corresponding to standard deviation of less than 0.3 m for the
 662 upscaled 90 m LIDAR pixel are not included.

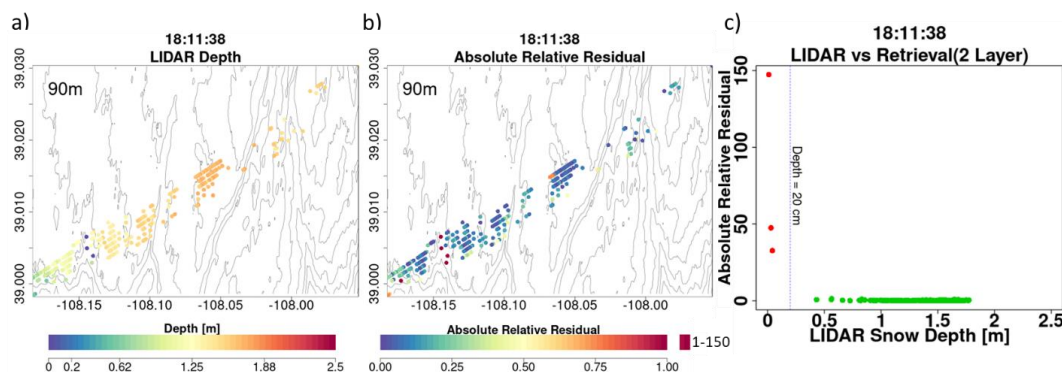
663



664

665 **Figure A10** - Histogram of snow depth (SD) from LIDAR, MSHM, and successful retrievals at 90 m using 1- and 2- layer
 666 snowpacks. The total number of pixels for each snow depth product is the same. Successful retrievals are for pixels with local
 667 incidence angles in the 30°- 45° range and relative residual backscatter (RRB) of less than 30% for each of the four flights (see
 668 Table 4). LIDAR SD in pixels with subgrid scale variability corresponding to standard deviation of less than 0.3 m for the
 669 upscaled 90 m LIDAR pixel are not included.

670

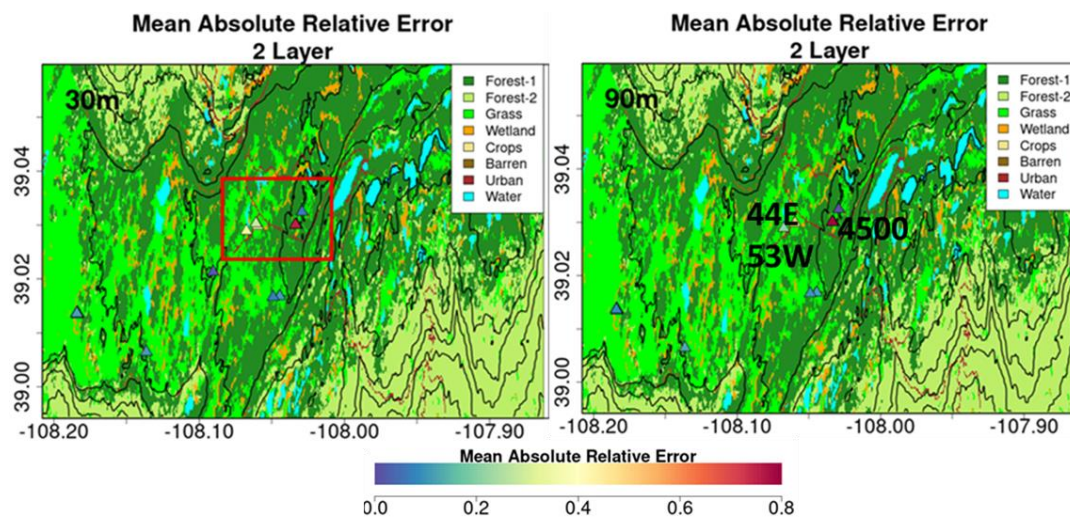


671

672 **Figure A11** - Analysis of unsuccessful retrievals for pixels with large mean snow depth residuals at 90 m resolution: a) Map of
 673 LIDAR snow depth highlighting in deep blue the locations where very shallow snow is attributed to measurement error. b) Note
 674 spatial agreement between shallow snow depth and very large residuals. c) There are only a few points at the edges of forests and
 675 shallow snow depths that are flagged not successful. The gray elevation contours are plotted every 50 m.

676

677



678

679 **Figure A12** – Spatial context for snow pits with very large absolute relative errors (MARE) calculated as the mean of the
680 relative difference between SWE retrievals within 100 m of the snow pit and the values at the snow pit. Locations with very large
681 errors (orange to red) are inside the red box marked in top plot. Snowpit 4500 is a region of complex land cover including
682 evergreen forest, a road and a pond. Snowpits 53W and 44E are close to each other on the same side of the road in expansive
683 grassland.

684

685 8. Competing Interests

686 The contact author has declared that none of the authors has any competing interests

687

688 9. References

689 Bateni, S. M., Margulis, S. A., Podest, E., and McDonald, K. C.: Characterizing Snowpack and
690 the Freeze–Thaw State of Underlying Soil via Assimilation of Multifrequency Passive/Active
691 Microwave Data: A Case Study (NASA CLPX 2003), *IEEE Trans. Geosci. Remote Sens.*, 53,
692 173–189, <https://doi.org/10.1109/TGRS.2014.2320264>, 2015.

693 Benjamin, S. G., Weygandt, S. S., Brown, J. M., Hu, M., Alexander, C. R., Smirnova, T. G., Olson,
694 J. B., James, E. P., Dowell, D. C., Grell, G. A., Lin, H., Peckham, S. E., Smith, T. L., Moninger,
695 W. R., Kenyon, J. S., and Manikin, G. S.: A North American Hourly Assimilation and Model
696 Forecast Cycle: The Rapid Refresh, *Mon. Weather Rev.*, 144, 1669–1694,
697 <https://doi.org/10.1175/MWR-D-15-0242.1>, 2016.

698 Berliner, L. M.: Physical-statistical modeling in geophysics: Physical-Statistical Modeling in
699 Geophysics, *J. Geophys. Res. Atmospheres*, 108, n/a-n/a, <https://doi.org/10.1029/2002JD002865>,
700 2003.

701 Bhattacharyya, A.: On a measure of divergence between two statistical populations defined by
702 their probability distributions". <https://doi.org/10.3390/rs12203422>, 2020.



- 703 Cao, Y. and Barros, A.P.: Weather-Dependent Nonlinear Microwave Behavior of Seasonal High-
704 Elevation Snowpacks, *Remote Sens.*, 12, 3422, <https://doi.org/10.3390/rs12203422>, 2020.
- 705 Cao, Y. and Barros, A. P.: Topographic controls on active microwave behavior of mountain
706 snowpacks, *Remote Sens. Environ.*, 284, 113373, <https://doi.org/10.1016/j.rse.2022.113373>,
707 2023.
- 708 Cao, Y., and Barros, A.P.: Indirect Estimation of Boreal Vegetation Contributions to SAR
709 Backscatter Measurements – Toward Operational Retrievals of Snow in Forest Areas. *Rem.*
710 *Sensing of the Environ.*, in review, 2023. ESS Open Archive, August 14, 2023,
711 <https://doi:10.22541/au.169200040.06589257/v1>, 2023.
- 712 Deems, J. S., Painter, T. H., and Finnegan, D. C.: Lidar measurement of snow depth: a review, *J.*
713 *Glaciol.*, 59, 467–479, <https://doi.org/10.3189/2013JoG12J154>, 2013.
- 714 Dobson, M., Ulaby, F., Hallikainen, M., and El-rayes, M.: Microwave Dielectric Behavior of
715 Wet Soil-Part II: Dielectric Mixing Models, *IEEE Trans. Geosci. Remote Sens.*, GE-23, 35–46,
716 <https://doi.org/10.1109/TGRS.1985.289498>, 1985.
- 717 Dobson, M., Ulaby, F., Hallikainen, M., and El-rayes, M.: Microwave Dielectric Behavior of
718 Wet Soil-Part II: Dielectric Mixing Models, *IEEE Trans. Geosci. Remote Sens.*, GE-23, 35–46,
719 <https://doi.org/10.1109/TGRS.1985.289498>, 1985.
- 720 Hallikainen, M., Ulaby, F., Dobson, M., El-rayes, M., and Wu, L.: Microwave Dielectric
721 Behavior of Wet Soil-Part I: Empirical Models and Experimental Observations, *IEEE Trans.*
722 *Geosci. Remote Sens.*, GE-23, 25–34, <https://doi.org/10.1109/TGRS.1985.289497>, 1985.
- 723 Huang, X. and Swain, D. L.: Climate change is increasing the risk of a California megaflood, *Sci.*
724 *Adv.*, 8, eabq0995, <https://doi.org/10.1126/sciadv.abq0995>, 2022.
- 725 Kang, D. H. and Barros, A. P.: Observing System Simulation of Snow Microwave Emissions Over
726 Data Sparse Regions—Part I: Single Layer Physics, *IEEE Trans. Geosci. Remote Sens.*, 50, 1785–
727 1805, <https://doi.org/10.1109/TGRS.2011.2169073>, 2012a.
- 728 Kang, D. H. and Barros, A. P.: Observing System Simulation of Snow Microwave Emissions
729 Over Data Sparse Regions—Part II: Multilayer Physics, *IEEE Trans. Geosci. Remote Sens.*, 50,
730 1806–1820, <https://doi.org/10.1109/TGRS.2011.2169074>, 2012b.
- 731 Kim, E., Gatebe, C., Hall, D., Newlin, J., Misakonis, A., Elder, K., Marshall, H. P., Hiemstra, C.,
732 Brucker, L., De Marco, E., Crawford, C., Kang, D. H., and Entin, J.: NASA’s snowex campaign:
733 Observing seasonal snow in a forested environment, in: 2017 IEEE International Geoscience and
734 Remote Sensing Symposium (IGARSS), 2017 IEEE International Geoscience and Remote
735 Sensing Symposium (IGARSS), Fort Worth, TX, 1388–1390,
736 <https://doi.org/10.1109/IGARSS.2017.8127222>, 2017.
- 737 Kim, R. S., Durand, M., Li, D., Baldo, E., Margulis, S. A., Dumont, M., and Morin, S.: Estimating
738 alpine snow depth by combining multifrequency passive radiance observations with ensemble



- 739 snowpack modeling, *Remote Sens. Environ.*, 226, 1–15, <https://doi.org/10.1016/j.rse.2019.03.016>,
740 2019.
- 741 Kuhnert, P. M. (2017). Physical-statistical modeling. In *Wiley StatsRef: Statistics Reference*
742 Online, pages 1–5. Wiley.
- 743 Li, D., Durand, M., and Margulis, S. A.: Estimating snow water equivalent in a Sierra Nevada
744 watershed via spaceborne radiance data assimilation, *Water Resour. Res.*, 53, 647–671,
745 <https://doi.org/10.1002/2016WR018878>, 2017.
- 746 Manickam, S. and Barros, A.: Parsing Synthetic Aperture Radar Measurements of Snow in
747 Complex Terrain: Scaling Behaviour and Sensitivity to Snow Wetness and Landcover, *Remote*
748 *Sens.*, 12, 483, <https://doi.org/10.3390/rs12030483>, 2020.
- 749 Martinec, J., Seidel, K., Burkart, U., and Baumann, R.: Areal modelling of snow water equivalent
750 based on remote sensing techniques., XX General Assembly IUGG in Vienna, 1991.
- 751 Mendoza, P. A., Musselman, K. N., Revuelto, J., Deems, J. S., López-Moreno, J. I., and McPhee,
752 J.: Interannual and Seasonal Variability of Snow Depth Scaling Behavior in a Subalpine
753 Catchment, *Water Resour. Res.*, 56, <https://doi.org/10.1029/2020WR027343>, 2020.
- 754 Metropolis, N., Rosenbluth, A. W., Rosenbluth, M., N., Teller, A., and Teller, E.: Equation of State
755 Calculations by Fast Computing Machines. *The Journal of Chemical Physics*, 21, 1087-1092,
756 <https://doi.org/10.1063/1.1699114>, 1953.
- 757 Mote, T. L., Grundstein, A. J., Leathers, D. J., and Robinson, D. A.: A comparison of modeled,
758 remotely sensed, and measured snow water equivalent in the northern Great Plains:
759 COMPARISON OF SNOW WATER EQUIVALENT, *Water Resour. Res.*, 39,
760 <https://doi.org/10.1029/2002WR001782>, 2003.
- 761 Musselman, K. N., Addor, N., Vano, J. A., and Molotch, N. P.: Winter melt trends portend
762 widespread declines in snow water resources, *Nat. Clim. Change*, 11, 418–424,
763 <https://doi.org/10.1038/s41558-021-01014-9>, 2021.
- 764 National Academies of Sciences, Engineering, and Medicine: Thriving on Our Changing Planet:
765 A Decadal Strategy for Earth Observation from Space. Washington, DC: The National Academies
766 Press. <https://doi.org/10.17226/24938>, 2018.
- 767 Painter, Thomas H., Berisford, Daniel F., Boardman, Joseph W., Bormann, Kathryn J., Deems,
768 Jeffrey S., Gehrke, Frank, Joyce, Michael, Laidlaw, Ross, Mattmann, Chris, McGurk, Bruce,
769 Ramirez, Paul, Richardson, Megan, and Skiles, S. McKenzie: ASO L4 Lidar Snow Depth 3m
770 UTM Grid, Version 1, <https://doi.org/10.5067/KIE9QNVG7HP0>, 2018.
- 771 Pan, J., Durand, M. T., Vander Jagt, B. J., and Liu, D.: Application of a Markov Chain Monte
772 Carlo algorithm for snow water equivalent retrieval from passive microwave measurements,
773 *Remote Sens. Environ.*, 192, 150–165, <https://doi.org/10.1016/j.rse.2017.02.006>, 2017.



- 774 Proksch, M., Mätzler, C., Wiesmann, A., Lemmetyinen, J., Schwank, M., Löwe, H., and
775 Schneebeli, M.: MEMLS3&a: Microwave Emission Model of Layered Snowpacks adapted to
776 include backscattering, *Geosci. Model Dev.*, 8, 2611–2626, [https://doi.org/10.5194/gmd-8-2611-](https://doi.org/10.5194/gmd-8-2611-777)
777 2015, 2015.
- 778 Rott, H., Cline, D. W., Duguay, C., Essery, R., Etchevers, P., Hajnsek, I., Kern, M., Macelloni,
779 G., Malnes, E., Pulliainen, J., and Yueh, S. H.: CoReH2O, a dual frequency radar mission for
780 snow and ice observations, in: 2012 IEEE International Geoscience and Remote Sensing
781 Symposium, IGARSS 2012 - 2012 IEEE International Geoscience and Remote Sensing
782 Symposium, Munich, Germany, 5550–5553, <https://doi.org/10.1109/IGARSS.2012.6352348>,
783 2012.
- 784 Sturm, M., Taras, B., Liston, G. E., Derksen, C., Jonas, T., and Lea, J.: Estimating Snow Water
785 Equivalent Using Snow Depth Data and Climate Classes, *J. Hydrometeorol.*, 11, 1380–1394,
786 <https://doi.org/10.1175/2010JHM1202.1>, 2010.
- 787 Tsang, L., Durand, M., Derksen, C., Barros, A. P., Kang, D.-H., Lievens, H., Marshall, H.-P., Zhu,
788 J., Johnson, J., King, J., Lemmetyinen, J., Sandells, M., Rutter, N., Siqueira, P., Nolin, A.,
789 Osmanoglu, B., Vuyovich, C., Kim, E., Taylor, D., Merkouriadi, I., Brucker, L., Navari, M.,
790 Dumont, M., Kelly, R., Kim, R. S., Liao, T.-H., Borah, F., and Xu, X.: Review article: Global
791 monitoring of snow water equivalent using high-frequency radar remote sensing, *The Cryosphere*,
792 16, 3531–3573, <https://doi.org/10.5194/tc-16-3531-2022>, 2022.
- 793 Villano, M., Ustalli, N., Dell’Amore, L., Jeon, S.-Y., Krieger, G., Moreira, A., Peixoto, M. N., and
794 Krecke, J.: NewSpace SAR: Disruptive Concepts for Cost-Effective Earth Observation Missions,
795 in: 2020 IEEE Radar Conference (RadarConf20), 2020 IEEE Radar Conference (RadarConf20),
796 Florence, Italy, 1–5, <https://doi.org/10.1109/RadarConf2043947.2020.9266694>, 2020.
- 797 Wiesmann, A. and Mätzler, C.: Microwave Emission Model of Layered Snowpacks, *Remote Sens.*
798 *Environ.*, 70, 307–316, [https://doi.org/10.1016/S0034-4257\(99\)00046-2](https://doi.org/10.1016/S0034-4257(99)00046-2), 1999.